OPTICAL PERFUSION AND OXYGENATION CHARACTERIZATION IN A LIVER PHANTOM

A Thesis

by

TRAVIS J. KING

Submitted to the Office of Graduate Studies of
Texas A&M University
in partial fulfillment of the requirements for the degree of

MASTER OF SCIENCE

December 2011

Major Subject: Biomedical Engineering

Optical Perfusion and Oxygenation Characterization in a Liver Phantom

OPTICAL PERFUSION AND OXYGENATION CHARACTERIZATION IN A LIVER PHANTOM

A Thesis

by

TRAVIS J. KING

Submitted to the Office of Graduate Studies of
Texas A&M University
in partial fulfillment of the requirements for the degree of

MASTER OF SCIENCE

Approved by:

Chair of Committee,	Gerard L. Coté
Committee Members,	Michael J. McShane
	Jun Kameoka
Head of Department,	Gerard L. Coté

December 2011

Major Subject: Biomedical Engineering

ABSTRACT

Optical Perfusion and Oxygenation Characterization in a Liver Phantom.

(December 2011)

Travis J. King, B.S., Louisiana Tech University

Chair of Advisory Committee: Dr. Gerard L. Coté

Continuous monitoring of blood perfusion and oxygenation is essential in assessing the health of a transplanted organ. Particularly, monitoring the perfusion and oxygenation of the organ during the two-week period after the transplant procedure is crucial in detecting a sustained loss in perfusion or a reduction in oxygen saturation before these changes render irreversible damage to the organ or patient. Pulse oximetry is a clinically accepted method of monitoring the arterial oxygen saturation of a patient in a non-invasive manner. Pulse oximeters exploit the wavelength-dependent absorption of oxygenated and deoxygenated hemoglobin to measure a patient's arterial oxygen saturation. However, traditional pulse oximeters do not provide perfusion information and produce erroneous oxygen saturation measurements under low perfusion levels.

An optical blood perfusion and oxygenation sensor, based on a modified reflectance pulse oximeter, has been developed for *in situ* monitoring of transplanted organs. To reduce the number of animal experiments, phantoms that mimic the optical and anatomical properties of liver parenchyma have also been developed. In this work, *in vitro* data was gathered from dye solutions mimicking oxygenated blood that were

pumped through single and multi-layer phantoms mimicking liver parenchyma and through a phantom mimicking the portal vein. A portion of the phantom data was compared to data collected from *in vivo* occlusion studies performed on female swine to assess the ability of the phantoms to mimic the response observed with changes in blood perfusion through liver parenchyma. Both the single layer and multilayer phantoms showed a similar response to changes in perfusion as the *in vivo* case. With each phantom, the signal increased linearly with increases in perfusion, but the multilayer phantom showed a higher sensitivity (approximately 30% higher) to changes in perfusion than the single layer phantom. This higher sensitivity would provide the ability to measure smaller changes in perfusion and increase the resolution of the sensor. Also, both parenchymal phantoms showed similar trends in the oxygenation studies, with the R value decreasing with increasing oxygenation. While the observations in this research demonstrate the ability to use both phantoms for *in vitro* experiments, the results show the multilayer phantom is a better option for mimicking perfusion because it displays similar occlusion patterns as the liver parenchyma *in vivo*, a higher sensitivity to changes in perfusion than the single layer phantom, and it is only slightly more complex in design (contains only two more layers of sinusoids) than the single layer phantom.

DEDICATION

I would like to dedicate this thesis to my mother, Ora L. King, for her guidance, support, love, and encouragement. Without her, I would not have had the desire or the courage to continue through this process. I would also like to dedicate this thesis to my family and friends who have continued to encourage me throughout life and while I was in graduate school. Without your support and encouragement, I doubt the completion of this thesis would ever have been possible.

ACKNOWLEDGEMENTS

I would like to express my deepest and most sincere gratitude to my advisor, Dr. Gerard L. Coté, for financial support and guidance throughout this process. Also, I would like to thank my committee members, Dr. McShane and Dr. Kameoka, for their guidance during this research process. Thanks also go to my friends and the students of the Optical Biosensing Laboratory for their moral support and for making my experience at Texas A&M University an enjoyable one. I am also grateful to my girlfriend for all of her support throughout this process and for helping me stay focused on writing and meeting deadlines to ensure the completion of this document. I would like to thank Tony Akl, a PhD student in the Optical Biosensing Laboratory for his suggestions and guidance for my experiments and data analysis. I wish to thank Dr. Ericson and his team at Oak Ridge National Laboratory for providing the system for use with gathering data for my experiments, Dr. Mark Wilson at the University of Pittsburgh and Veterans Affairs Medical Center (Pittsburgh, PA) for his clinical support, and Dr. McShane and Ruiqi Long for providing the phantoms for use with the *in vitro* experiments. I would also like to thank the National Institutes of Health for its financial support without which the continuation of this project would not have been possible.

Throughout my time in school, my parents, particularly my mother, have encouraged me to continue to pursue my education even when at times the challenges presented seemed insurmountable. I am grateful to them and to my family for all of their

support and encouragement throughout school and all other challenges I have faced in my life.

TABLE OF CONTENTS

CHAPTER Page

LIST OF FIGURES

FIGURE Page

LIST OF TABLES

TABLE Page

CHAPTER I

INTRODUCTION

According to the Scientific Registry of Transplant Recipients (SRTP) and the Organ Procurement and Transplantation Network (OPTN), the number of patients on the waiting list for a liver transplant as of July 2011 is 16,169, but the number of liver transplant procedures performed in 2011 is 2,037 (based on OPTN data as of July 20, 2011). These numbers suggest that the number of available donor organs is failing to meet the patient demands. One-year graft survival rates from living and deceased donors were 84.3% and 86.6%, respectively, between 2006 and 2007 [1]. Therefore, there is a need to minimize graft loss and increase the success rate of liver transplant procedures. This increase in the success rate should lead to a decrease in the demand for livers.

A means of monitoring the status of the transplanted organ over time is important in noticing trends that suggest a failing graft and organ. A common cause of organ failure is complications due to graft failure, and a common cause of graft failures is ischemia, which is often caused by Hepatic Artery Thrombosis (HAT) and Portal Vein Thrombosis (PVT) [2]. Due to a limited availability of cadaveric organs and an increasing number of patients being added to the waiting each year list, portions of liver from living donors are being used in transplant procedures. However, the use of this method increases the likelihood that PVT or HAT will occur. A prolonged decrease in blood flow to the transplanted organ can result in loss of organ function, which can be

---

This thesis follows the style of Biomedical Optics Express.

hazardous to the patient and will require additional surgical procedures to be performed to save the organ or, in the most extreme cases, save the patient. The 7-10 days following the transplant procedure proves to be the most critical in assessing the health of the organ. It is within this time period that physicians can assess the health of the organ and determine if additional surgical procedures are necessary to save the organ. The ability to monitor blood perfusion to the organ during this critical time period will allow physicians to detect trends in the perfusion that suggest a failing organ and address the issue before the damage to the organ becomes irreversible. The increase in graft survival will be beneficial in preventing multiple transplant procedures from being performed, which will decrease the loss of donor organs, and decreasing the loss of donor organs is important given the number of patients on the waiting list.

In order to detect blood perfusion and oxygenation of an implanted organ, the Optical Biosensing Laboratory at Texas A&M University, in collaboration with Oak Ridge National Laboratories and the University of Pittsburgh is developing an *in vivo* sensor. The sensor, based on a modified reflectance pulse oximeter, is envisioned to be the size of a quarter to allow it to be implanted onto the surface of the transplanted organ during the recovery period. The signal measured by the sensor is proposed to be sent to a nearby desktop computer via wireless telemetry for signal processing [3-7].

To facilitate sensor design while minimizing animal experiments, it is useful to test the sensor on a phantom that mimics the optical and flow properties of the liver parenchyma. A phantom developed by Ruiqi Long *et al.* has been shown to mimic the optical and anatomical properties of the liver parenchyma in the NIR wavelength range

(630-1000 nm)[8]. The primary goal of this thesis is to assess the ability of the opto-fluidic phantoms developed by Ruiqi Long *et al.* to mimic the flow properties of the portal vein and liver parenchyma. To evaluate how effectively the phantoms mimic the flow properties of liver parenchyma, *in vitro* perfusion studies must be performed with the phantoms and the prototype sensor. The data gathered during the *in vitro* studies will be compared to data acquired from *in vivo* pig studies. A secondary goal of this thesis is to study the effects of varying oxygenation on the sensor performance. Data will be acquired during *in vitro* studies on the parenchymal phantoms. To fulfill the goals of this research, the following specific aims are proposed:

- **Specific Aim 1: Complete flow system for *in vitro* parenchymal and portal vein phantoms.**

  We will develop a flow system along with a dye solution that mimics the absorptive properties of hemoglobin to incorporate pulsatile flow through a phantom that mimics the optical and anatomical properties of the liver for use in preliminary studies. Studies will be conducted on phantoms that mimic the optical and anatomical properties of both the liver parenchyma and portal vein.

- **Specific Aim 2: Compare flow characteristics of the parenchymal and portal vein phantoms to *in vivo* porcine parenchyma flow characteristics.**

  In this work, the ability of the parenchymal and portal vein phantoms to mimic the flow properties of the liver will be assessed. The measured signal from the phantoms will be compared with the signal measured from porcine liver.

In the following work, the ability of phantoms developed by Long *et al* to mimic the flow properties of the portal vein and of liver parenchyma will be assessed. Overall, it was shown that the phantoms effectively mimic the flow properties of liver parenchyma. Specifically, both the single and multilayer parenchymal phantom showed similar responses to changes in perfusion. However, the multilayer phantom had a greater sensitivity to changes in perfusion a higher signal. Therefore, while both parenchymal phantoms can be used to facilitate sensor design, it is more applicable to use the multilayer phantom because it more closely mimics the anatomical properties of liver parenchyma. The portal vein phantom also showed a similar response to *in vivo* perfusion studies. It was concluded in this work that the phantoms mimicking the liver parenchyma and the portal vein can be used to facilitate sensor design.

CHAPTER II

BACKGROUND

The first section of this chapter covers the anatomy of hemoglobin, the physiology of oxygen transport, and the anatomy and physiology of the liver. The next section covers current methods employed to monitor tissue perfusion followed by a section on pulse oximetry—it's history, limitations, and implementation in the clinical setting.

2.1 Anatomy and physiology

2.1.1 Oxygen transport

Oxygen is one of the most essential elements for the human body. It is responsible for maintaining the proper functioning of each cell in the body, and most importantly, it is essential for the respiratory process, which is the basis for how we use stored energy. Oxygen is transported to the cells of the body through hemoglobin, a molecule present in red blood cells. This phenomenon makes hemoglobin one of the most essential molecules in the human body. The oxygen transport process begins with the breathing of air into the lungs. Blood passing through the lungs is oxygenated by the air that is breathed into the lungs and is transported to various parts of the body. The cells of the body use the oxygen present in the hemoglobin, and the resultant deoxygenated blood is returned to the lungs to be oxygenated once again. The lungs serve to allow the exchange of gases in the blood resulting in the blood ridding itself of carbon dioxide (a byproduct of respiration) and replenishing itself with oxygen. The oxygenated blood is then recirculated throughout the body [9, 10].

Hemoglobin is the most important molecule present in red blood cells because it allows oxygen to be transported to the cells of the body. A hemoglobin molecule is a protein that consists of four heme groups each bound to a polypeptide chain. Each of the heme groups in a hemoglobin molecule contains an atom of iron that allows an oxygen molecule to bind to the heme group. Therefore, a single hemoglobin molecule can bind four oxygen molecules. The polypeptide chains bound to each of the four heme groups are collectively called a globin [9, 10]. Hemoglobin exists in many forms, but the two most prevalent forms in the bloodstream are oxygenated (HbO_2) and deoxygenated (Hb) hemoglobin. Oxygenated hemoglobin is reddish in color and absorbs more light in the near infrared (NIR) wavelength range than in the red and far red wavelength range. In contrast, deoxygenated hemoglobin is bluish in color and absorbs more light in the red and far red wavelength range than in the NIR wavelength range. This absorption difference is exploited in pulse oximetry, which is a clinically accepted method to non-invasively measure arterial oxygen saturation [11, 12]. The partial pressure of oxygen (PO_2) is directly related to the amount of oxygen dissolved in the blood. Some oxygen may be present in the blood plasma, but this oxygen content only represents approximately 3% of the total oxygen supplied to the cells by the blood. The remaining 97% of oxygen present in the blood is bound to hemoglobin molecules, and a measure of the ratio of the amount of oxygen bound to the hemoglobin to the oxygen carrying capacity of the hemoglobin is known as oxygen saturation (SO_2) [9, 10]. Since a majority of the oxygen is transported by hemoglobin molecules, measures of the amount

of blood supplied to various parts of the body as well as the oxygenation of the blood being transported are important in assessing the health of a patient.

2.1.2 Liver anatomy and physiology

The liver is an essential organ in the body, and its most important functions lie within three categories: metabolic functions, secretory and excretory functions, and vascular functions. The vascular function is responsible for the storage and filtration of blood, and this research project focuses on the vascular function of the liver. The liver receives blood from two sources, the hepatic artery and the portal vein. The hepatic artery supplies oxygenated blood at a rate of 350 mL/min (~25% of the total blood volume), and the portal vein supplies venous blood at a rate of 1100 mL/min (~75% of the total blood volume). Blood flow through the liver averages about 1450 mL/min, which is approximately 29% of the cardiac output of a resting adult. The liver can also serve as a blood reservoir capable of storing an additional 0.5 to 1 liter of blood when high pressure in the right atrium of the heart causes back pressure in the liver—a common symptom of congestive heart failure [9, 10, 13].

The basic functional unit of the liver is a structure known as the *liver lobule*. A liver lobule is hexagonally structured, several millimeters in depth, and ranges from 0.8 to 2 millimeters in diameter. The length of each side of the liver lobule ranges from 0.5 to 1 millimeter. The average liver consists of roughly 1 million liver lobules, and each liver lobule consists of portal triads, sinusoids, hepatocytes, and the central vein. The *portal triads* (a total of six per lobule) are located at the point where two edges of the hexagonally structured liver lobules meet, and each triad consists of branches of the

portal vein, hepatic artery, and bile canaliculi. The sinusoids are small channels lined with hepatocytes that allow blood to drain from the portal triads into the central vein. It is within these channels of the sinusoids that the exchange of oxygen and other nutrients takes place. Located at the center of the liver lobule is a branch of the central vein, which empties into the hepatic vein. The hepatic vein empties into the superior vena cava where the blood mixes with other venous blood from the periphery of the body [9, 10, 13]. The primary goal of this research project is to assess the effectiveness of liver phantoms developed by Long *et al.* [8] in mimicking the flow properties of actual liver tissue.

2.2 Current monitoring methods

Current monitoring methods include Laser Doppler Flowmetry, Thermal Diffusion, Computed Tomography (CT), Diffuse Correlation Spectroscopy (DCS), Diffuse Reflectance Spectroscopy (DRS), Magnetic Resonance Imaging (MRI), and Near Infrared Spectroscopy (NIRS) with Indocyanine Green (ICG) as a contrast agent [14-45]. Laser Doppler Flowmetry measures perfusion by correlating the Doppler Shift induced by moving objects to blood flow. However, this technique is susceptible to high motion artifact making it not suitable for implantation [15]. Thermal Diffusion is a technique that measures local tissue perfusion based on thermal convection. A typical thermal diffusion probe consists of a proximal and a distal thermistor. The proximal thermistor measures the baseline temperature of the surrounding tissue, and the distal thermistor is powered to induce a slight temperature increase in the local tissue volume. The power required to maintain this increase in temperature is a function of blood

perfusion within the tissue volume [46, 47]. Although this technique is capable of measuring perfusion in localized tissue, it is difficult to apply directly to blood vessels, which would be useful in monitoring graft health. Indocyanine Green is a dye with a characteristic absorption peak near the hemoglobin isobestic point (805 nm). It's clearance from the plasma by liver tissue is measured by Near Infrared Spectroscopy (NIRS), and its plasma concentration vs. time can be used to predict perfusion in the liver [48]. A problem with the aforementioned techniques is the lack of provision of oxygenation information which is essential information when assessing the health of a graft and of the liver tissue. DCS and DRS are often combined to simultaneously measure blood perfusion and oxygenation. DCS measures the decay rate of an electric field autocorrelation function generated when light is multiply scattered from turbid media, such as blood, and correlates this decay rate to the flow rate of the blood. While the DCS and DRS devices are capable of measuring blood perfusion and oxygenation, the devices have not been sufficiently miniaturized for implantation [30, 34, 49]. CT and MRI, while capable of measuring blood perfusion, involve the use of a contrast agent to measure flow, are not feasible for implantation, and do not provide information on oxygenation. While the aforementioned methods are capable of monitoring blood perfusion in the liver under normal and adverse conditions (i.e. cirrhosis, partial, and total vessel occlusion), due to size, cost, need for a contrast agent, and/or lack of oxygenation information, they are not suitable for implantation and for continuous, real-time monitoring of perfusion over a two-week period.

2.3 Pulse oximetry

Optical-based monitoring techniques provide a means to monitor blood perfusion and oxygenation in a minimally invasive manner. One specific method that has been clinically accepted as a means for monitoring tissue oxygenation is pulse oximetry. Throughout the past two decades, pulse oximetry has become increasingly used to monitor tissue oxygenation in the clinical setting [11, 50-66].

2.2.1 History of pulse oximeters

The first documented use of light to measure blood oxygenation dates back to the late 1800's where the reduction of red light transmitted or reflected through the tissue of a hand was recorded by a physicist named Karl von Vierordt in 1874 [63]. The first oximeter was invented during World War II by a physiologist named Glenn Allen Milikan. Initially invented as a means to measure the arterial oxygen saturation of pilots, the first oximeters were heavy, cumbersome to transport, required extensive calibration before each use, and were limited to use on the earlobe. Also, the Milikan invention did not take into account the presence of other light-absorbing species in the earlobe. Therefore, calibration of his device required the earlobe to be cuffed and rendered bloodless to obtain the background signal due the presence of additional absorbers such as skin, cartilage, and other tissues. Also, to eliminate the absorption due to venous blood, the earlobe was heated to 44^{o} C, and a measurement was taken on a hyperemic ear that consisted of arterial blood only [67]. Two significant improvements to the oximeter were made in the 1970's that drastically improved the accuracy and portability of the device. The first improvement was made by Hewlett-Packard Corporation and

featured the use of multiple wavelengths of light to measure oxygenation [67]. The "pulse oximeter" was discovered by Takuo Aoyagi in the mid 1970's. He noticed that dyes injected into the blood stream showed a pulsatile absorption and that the amplitude of the pulsations was dependent on the arterial oxygen saturation of the patient [63]. With the invention of the pulse oximeter, the need for extensive calibration, such as in the Milikan case, was eliminated. However, as with the Milikan invention, this device was limited to use on the earlobe and was therefore cumbersome to use. The second improvement was made by an engineer named Scott Wilber, who used solid state light emitting diodes (LEDs) as the light source and a photodiode as the detector [67]. This improvement reduced the size of the device and increased its portability. Currently, pulse oximeters are clinically accepted as a means for non-invasively measuring arterial oxygen saturation [11, 12, 50].

2.2.2 Principle of pulse oximetry

Oximetry is a technique that utilizes the absorption difference between Hb and HbO_2 in the far red and near infrared (NIR) wavelength range. Light within the 600-1000 nm wavelength range is capable of penetrating fairly deeply into tissue. Due to the optical properties of tissue within this wavelength range, the reflectively of light within the 600-1000 nm wavelength range can be used to measure the perfusion and oxygenation of blood within the tissue volume being probed. Oximetry utilizes the technique of measuring the reflectivity or transmission (based on the differences in the absorption of Hb and HbO_2) of light through tissue and correlating the measured reflectivity or transmission to tissue oxygenation.

Pulse oximetry utilizes the same principles as oximetry in conjunction with a unique feature of the circulatory system—the pulsatile signal generated by arterial blood. The pulsatile signal generated by the arterial blood is relatively independent of tissue, venous blood, capillary blood, and non-pulsatile arterial blood. As arterial blood is pulsed through the body, the absorption of light in the far red and NIR wavelength ranges increases and decreases with each cardiac cycle. The increase and decrease in the absorption with each cardiac cycle generates an alternating current (AC) signal that is used to calculate the oxygenation of the arterial blood. Traditional pulse oximeters used LEDs that emitted at 660 nm (red) and 940 nm (infrared) due to the absorption properties of Hb and HbO_2 at these two wavelengths (Figure 1). The ratio of absorbances at these two wavelengths is used to form a calibration curve that is used to estimate the SaO_2 of the patient. The ratio, R (Equation 1), is calibrated empirically against a direct measurement of SaO_2 from volunteers. The algorithm derived from this empirical calibration is used in the signal processing of the pulse oximeter to estimate the patient's oxygen saturation.

$$R = \frac{\text{Absorbance}_{\text{Red}}}{\text{Absorbance}_{\text{IR}}} \qquad (1)$$

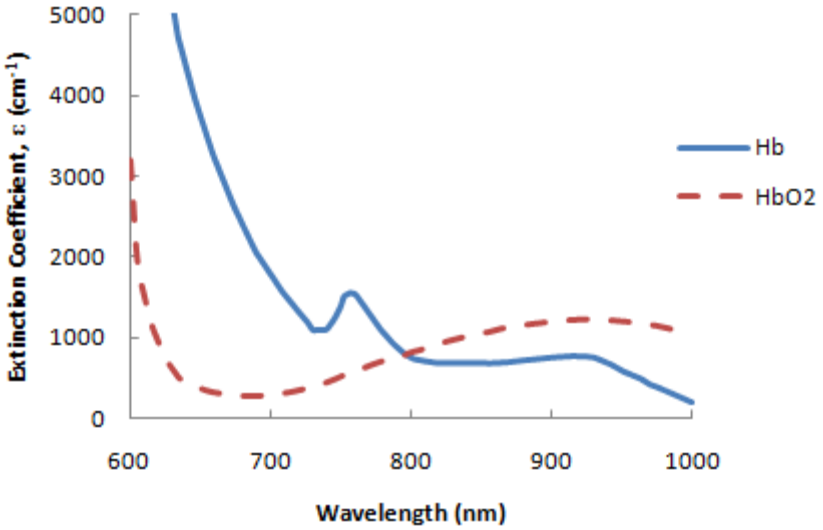

Figure 1: Extinction coefficients of Hb and HbO_2 [68].

The measurement technique of pulse oximeters is based on the Beer-Lambert Law, which relates the intensity of light transmitted through a material to the optical properties (particularly the absorption and scattering) of the material. In the case of a liquid, the Beer-Lambert Law relates the intensity of light transmitted through the solution to the concentration of solute present in the solution. For liquids, the Beer-Lambert Law can be written as

$$I = I_0 e^{-\varepsilon CL} \qquad (2)$$

where I and I_0 represent the intensity of the transmitted and incident light, respectively. ε ($mmol \cdot L^{-1} \cdot cm^{-1}$) is the wavelength-dependent molar extinction coefficient, C ($mmol \cdot L^{-1}$) is the concentration of the solute, and L (cm) is the path length of the light through the solution [69]. Assuming that the material is not a highly scattering medium, ε can represent the absorption of the material. However, for highly scattering mediums, ε is a

function of the absorption, μ_a (cm^{-1}), and scattering, μ_s (cm^{-1}), properties of the material. It must be noted that the Beer-Lambert Law assumes that the sum of the transmitted and absorbed light is equal to the incident light. It does not account for light that is reflected at the surface of the medium.

Early oximeters used tissue as the "cuvette" containing the hemoglobin for measurement of its absorption properties (Figure 2). However, tissue contains many other absorbers in addition to arterial blood, such as melanin, venous and capillary blood, and bone. Pulse oximeters are capable of distinguishing between pulsatile arterial blood and other absorbers by utilizing the pulsatile nature of arterial blood. Arterial blood pulses through the body as a result of the expansion of the arteriolar bed during systole, and this measured pulsatile signal can be viewed as an AC signal. The absorbance from materials other than pulsatile arterial blood is constant, and can be viewed as a direct current (DC) signal.

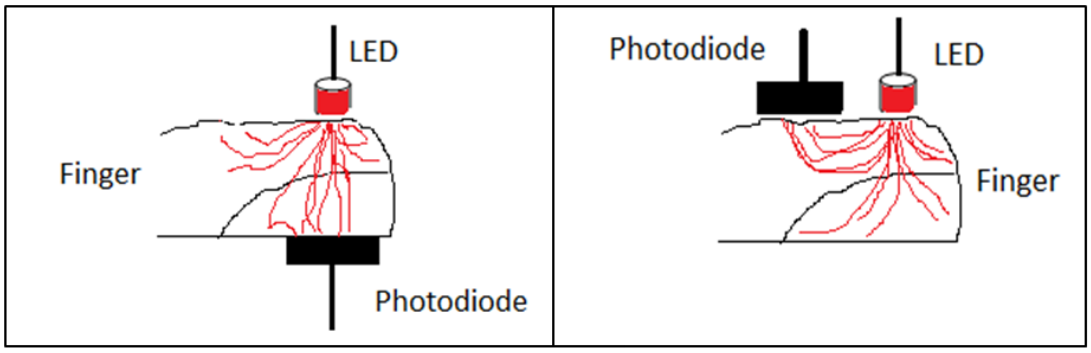

Figure 2: Transmission (left) and reflectance (right) pulse oximetry.

The increase in arteriolar volume during systole causes an increase in the optical path length of the light and results in an increase in the absorption. It must be noted that the technique of pulse oximetry makes a critical assumption—that all pulsatile absorbance is due to pulsatile arterial blood. Any other sources of pulsatile absorbance will result in an error in the measurement of arterial oxygen saturation. The height of the AC signal at the red and infrared wavelengths varies as a function of oxygenation (Figure 3).

The variance in the AC signal as a function of oxygenation is due to the difference in the absorption properties of Hb and HbO_2 at these wavelengths. Therefore, the ratio, R, can be rewritten as follows

$$R = \frac{AC_{Red}/DC_{Red}}{AC_{IR}/DC_{IR}} \qquad (3)$$

This ratio is related to hemoglobin oxygen saturation (S_aO_2). The oxygen saturation measured by the pulse oximeter (SpO_2) is derived from the calibration curve that relates R to arterial oxygen saturation. Figure 4 shows a theoretical calibration curve for a typical pulse oximeter. The S_aO_2 is a function of R, and can be written as follows:

$$S_aO_2(R) = \frac{\varepsilon_{Hb}(\lambda_R) - \varepsilon_{Hb}(\lambda_{IR})R}{\varepsilon_{Hb}(\lambda_R) - \varepsilon_{HbO_2}(\lambda_R) + \left[\varepsilon_{HbO_2}(\lambda_{IR}) - \varepsilon_{Hb}(\lambda_{IR})\right]R} \times 100\% \qquad (4)$$

where $\varepsilon_{Hb}(\lambda_R)$ and $\varepsilon_{HbO2}(\lambda_R)$ are the extinction coefficients of Hb and HbO_2, respectively, at the red wavelength, and $\varepsilon_{Hb}(\lambda_{IR})$ and $\varepsilon_{HbO2}(\lambda_{IR})$ are the extinction coefficients of Hb and HbO_2, respectively, at the infrared wavelength.

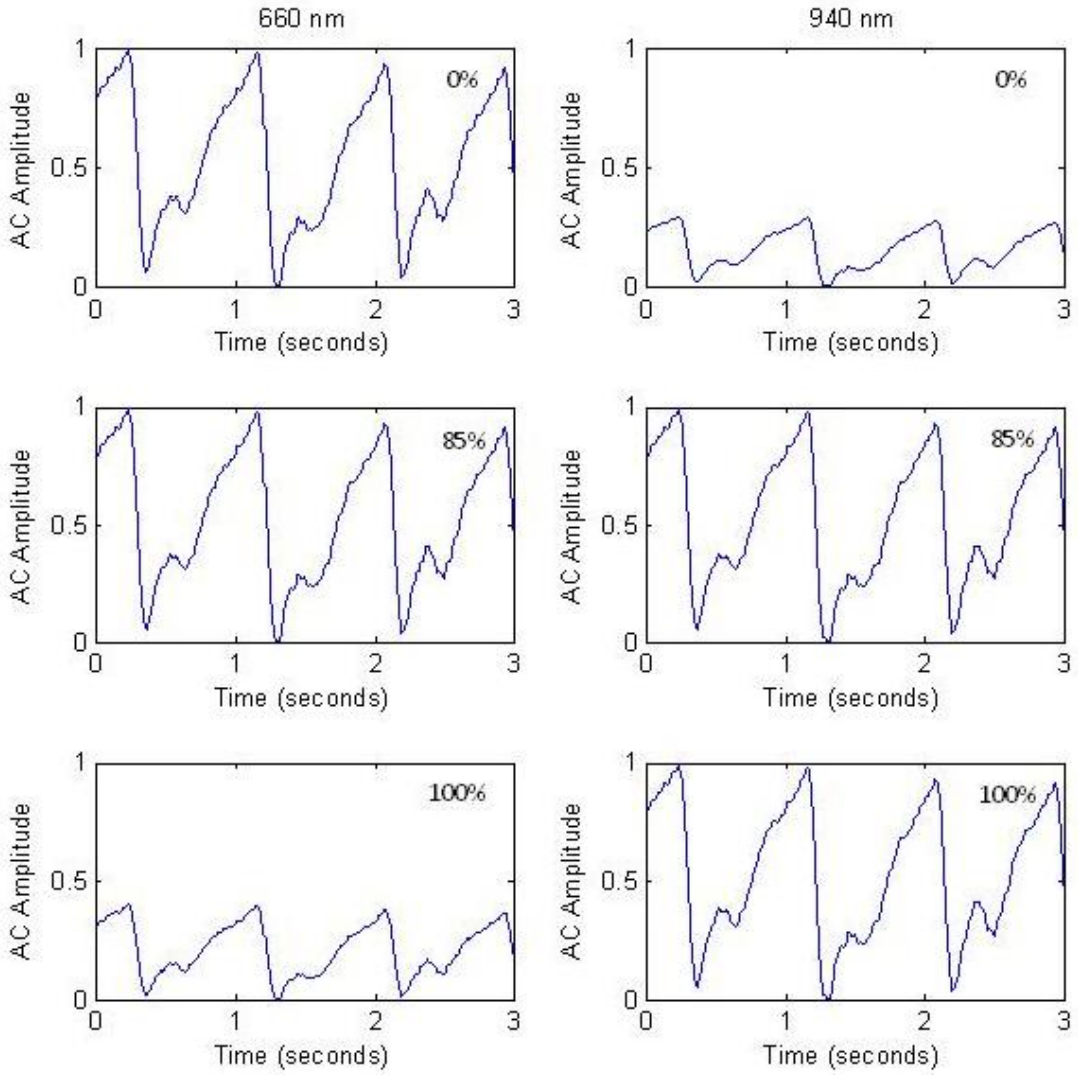

Figure 3: Sinulated red (660 nm) and infrared (940 nm) AC signals at different arterial oxygen saturations[1].

[1] Simulation performed with MatLAB (Mathworks, Inc.)

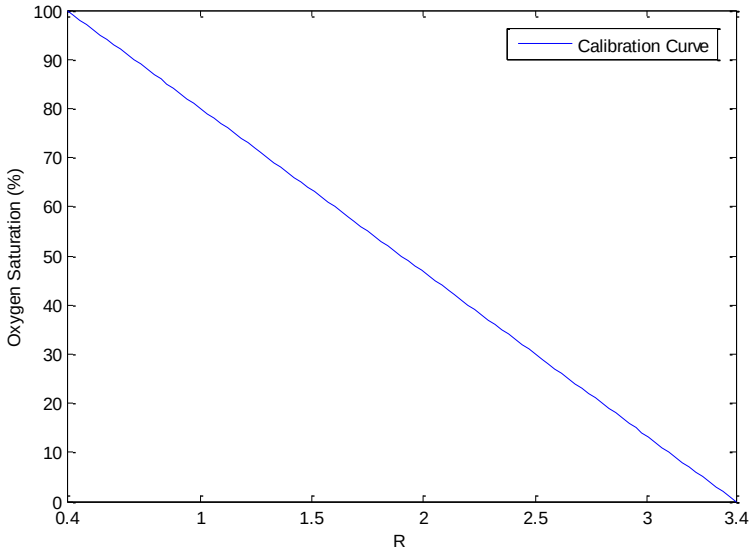

Figure 4: Typical calibration curve for a pulse oximeter.

2.2.3 Clinical applications of pulse oximeters

Pulse oximeters are useful, non-invasive tools used to monitor the arterial oxygen saturation, heart rate, and blood perfusion of patients in the clinical setting. One of the more common uses for pulse oximetry is arterial oxygen saturation monitoring during the administration of general anesthesia. In this setting, the pulse oximeter is valuable because it is capable of rapidly detecting hypoxia ($SaO_2 < 90\%$) and alerting the anesthesiologist so that oxygen can be administered in a timely manner. Among other uses of pulse oximeters are fetal oxygenation monitoring, monitoring of arterial oxygen saturation during sleep apnea, and monitoring of arterial oxygen saturation of patients being transported from the operating room to the recovery room [58, 59, 65, 70].

2.2.4 Limitations of pulse oximeters

Low oxygen saturation, motion artifact, low perfusion, and the presence of other species of hemoglobin are a few factors that may result in an inaccurate reading in pulse oximetry [67]. Pulse oximeters are designed to distinguish between two species of hemoglobin, HbO_2 and Hb, by employing two wavelengths of light. Pulse oximeters work well when HbO_2 and Hb are the only absorbing species of hemoglobin in the blood. However, the presence of alternative absorbing species of hemoglobin, mainly carboxyhemoglobin (COHb) and methoxyhemoglobin (MetHb), cause pulse oximeters to display incorrect oxygen saturation information. COHb, due to its absorption properties is seen as additional HbO_2 by pulse oximeters. MetHb is seen as both Hb and HbO_2 due to its aborbance in both the red and infrared wavelength range. The presence of a substantial amount of MetHb results in a false oxygen saturation value of 85% [67]. One technique that can be employed to eliminate the effects of COHb and MetHb is the use of additional wavelengths of light to distinguish between the different species of hemoglobin. The use of additional wavelengths of light provides the device with an independent measurement of the other species so that their absorbance can be subtracted from the Hb and HbO_2 absorbances. However, this adds to the complexity of the device [51].

Motion artifact is a significant source of error in pulse oximeters. The presence of motion artifact can either obscure the true photoplethysmographic signal or cause the device to interpret the motion artifact as the true photoplethysmographic signal. Another effect of motion artifact is a decrease in signal-to-noise ratio [71]. The misinterpretation

of data resulting from motion artifact can lead to inaccurate readings, false alarms, and missed true alarms. Various methods have been employed to combat the effects of motion artifact in pulse oximetry, but have resulted in little success [71, 72].

Developing an implantable sensor that utilizes light within the 600-1000 nm wavelength range provides a minimally invasive way to continuously monitor blood perfusion and oxygenation of an implanted organ. Issues with biocompatibility that often arise with implanted devices and sensors can be bypassed by coating the sensor in a biocompatible, optically transparent material. Development of such a sensor system would aid in reducing the amount of failed transplant procedures and should aid in decreasing the amount patients on the waiting list for organ transplants.

CHAPTER III

MATERIALS AND METHODS

The first section of this chapter provides a brief description of the sensor system design. The second section provides a description of the *in vitro* system setup used to perform experiments on the portal vein phantom and single layer and multilayer parenchymal phantoms, and the final section provides a description of the *in vivo* setup used for animal studies.

3.1 Sensor system design

The sensor system used during the *in vitro* experiments features a custom probe design used to measure oxygenation and perfusion of an organ by measuring backscattered light intensity. The sensor system delivers three wavelengths of light (735 nm, 805 nm, and 940 nm) via a three-LED light source (Epitex, L660/735/805/940-40B42-C-I), and the backscattered light is detectetd with a silicon photodetector (Hamamatsu, S2833-01). The three wavelengths of light emitted by the light source exploit the wavelength-dependent absorption of Hb and HbO_2 to extract oxygenation and perfusion information. A spherical glass lens is placed over the light source so that each of the wavelengths of light is directed onto the same tissue volume. The three-wavelength source is multiplexed in time and modulated via a unit developed by Oak Ridge National Laboratories (ORNL) to minimize power consumption and to eliminate background noise measured by the photodetector from ancillary light sources. The unit contains four anterior input channels, allowing for the detection of four signals with four separate probes, and eight posterior analog BNC inputs for detection of signals collected

from external sources. The analog BNC inputs provide a convenient interface for collecting time-correlated data from additional instruments such as Laser Doppler flow meters or thermal dilution monitors while gathering perfusion and oxygenation data. Several source-detector spacings for the probes (2 mm, 4 mm, 6 mm, 8 mm, and 10 mm) were available for use with the *in vitro* experiments.

The probe head is tethered to a box containing the power supply and the circuitry for modulation of the source light and demodulation of the detected signal. The circuitry consists of a demodulation circuit and a series of analog filters to separate the AC portion of the measured signal from the direct current (DC) portion. The analog output of the sensor electronics is input into a National Instruments data acquisition module (National Instruments; USB 6255) where it is then transferred to LabVIEW software (National Instruments) via a USB cable. A LabVIEW data acquisition program was written by ORNL to collect, display, and store the data in real time. The LabVIEW program provides the user with the ability to monitor the status of the four analog input channels as well as the external channels simultaneously or to monitor the status of an individual channel in more detail. Data sent to the LabVIEW program is stored in a text document for future analysis.

3.2 *In vitro* system setup

To assess the optical coupling and compliance of the phantom and to gather perfusion and oxygenation data, an *in vitro* system was setup for the single and multilayer parenchymal phantoms as well as the portal vein phantoms. The parenchymal phantoms were designed to imitate the case where the probe is placed on the surface of

the liver, and the portal vein phantoms were designed to imitate the case where the probe is placed on the portal vein just as it enters the liver.

3.2.1 Phantom design

The Polydimethylsiloxane (PDMS) based portal vein phantoms were prepared by mixing 437.4 mg of 0.5-1 µm Al_2O_3 powder (99.99% purity, Inframat ® Advanced Materials^{TM}), 120 mg of 100 nm Al_2O_3 powder (99.99% purity Inframat ® Advanced Materials^{TM}), 4.01 µL of black India Ink (Higgins, Black India 4415), 120 µL of blue food coloring (Wilton ®), and 60 mL of PDMS resin (SYLGARD ® USA). Long *et al*. has shown the ability of this mixture to mimic the optical properties of liver tissue in the far red and near infrared (NIR) wavelength range[8]. The mixture was sonicated and stirred until homogenous, and 6 mL of curing agent was added at a volumetric ratio of 1:10. The mixture containing the curing agent was stirred and cast into a plastic mold (Petri Dish approximately 40 mm in diameter). For the portal vein phantoms, a rigid plastic tube approximately 8 mm in diameter was inserted into the mold. A vacuum was applied to remove any bubbles that may have been present in the mixture, and then the mixture was allowed to cure for 2 hours in an oven at 65^{o}C to crosslink the PDMS. After the mixture cured, the rigid plastic tube was removed, and a compliant portal vein phantom resulted. For the non-compliant portal vein phantom, the rigid plastic tube was allowed to remain in the mold after the PDMS mixture cured. Figure 5 displays a front and side view of the PDMS based portal vein phantom and multi-layer parenchymal phantom.

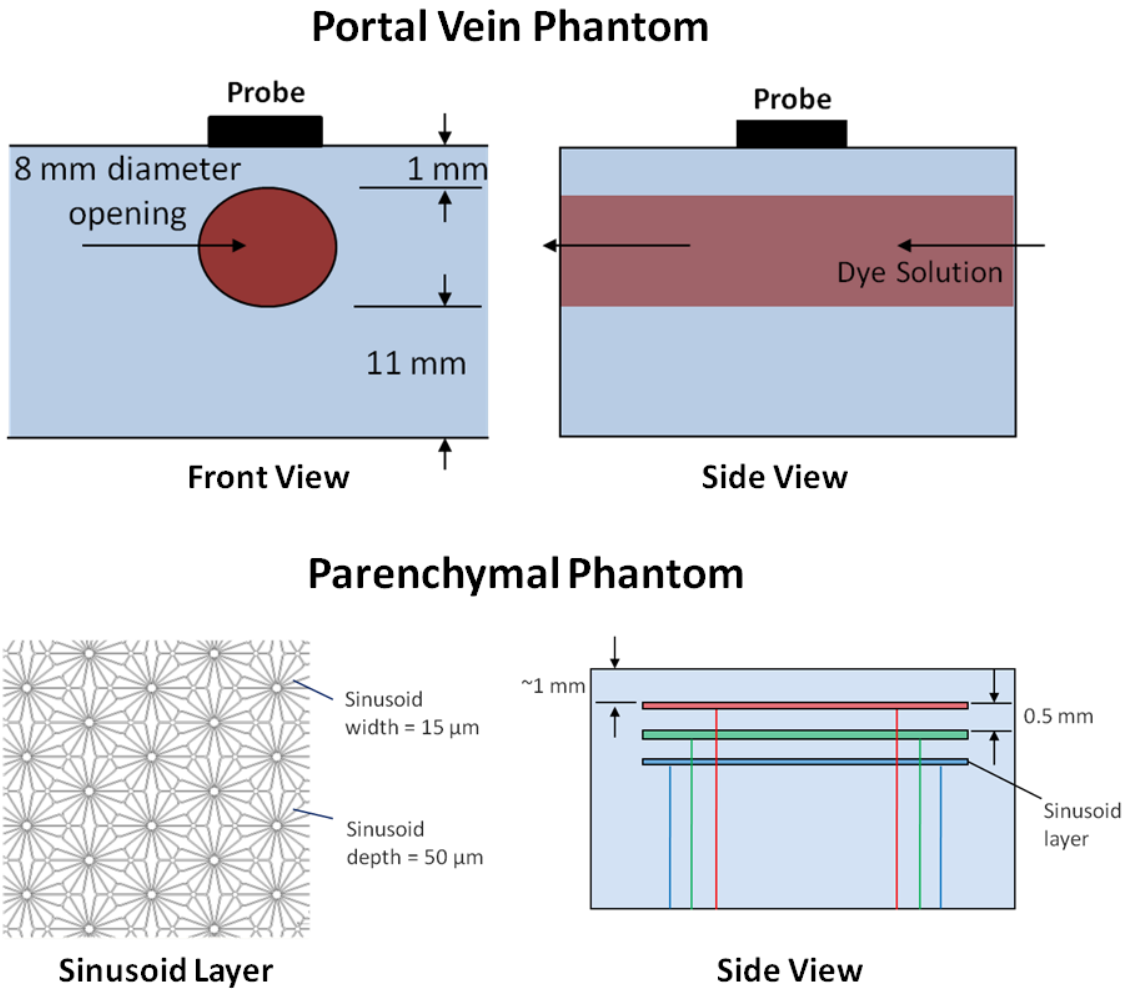

Figure 5: Schematic of the PDMS based compliant portal vein phantom showing the probe placed on top and a schematic of the multi-layer parenchymal phantom showing the design of the sinusoid layers and their location within the PDMS.

For the parenchymal phantoms, the same mixture used to construct the portal vein phantoms was employed. However, instead of containing a tube through the center, the phantoms contain microfluidic channels mimicking the liver sinusoids. A two-dimensional pattern of micro-fluidic channels mimicking the hexagonal sinusoids was

designed with computer-aided design (CAD) software (Rhinoceros 4.0). The design for the single layer parenchymal phantom consisted of one layer of sinusoids, and the design for the multi-layer parenchymal phantom consisted of three layers of sinusoids. The channels were cast into the PDMS mold using soft lithography. The PDMS mixture on the micro-patterned mold was degassed to remove any bubbles present between the channels. Holes were drilled through the thicker underside of the phantom in such a manner that they terminated at the ports of the microfluidic channels, and flat-tipped 20-guage needles (VWR, cat. # KT868280-2001) were inserted into the ports to allow dyes mimicking the absorbance of oxygenated and deoxygenated hemlglobin at our wavelengths of interest to be pulsed through the microfluidic channels. The width and height of the microfluidic channels are 15 μm and 50 μm, respectively.

3.2.2 Dyes mimicking hemoglobin absorption properties

To avoid handling whole blood, which needs to be placed in a temperature and pH-controlled environment and requires oxygenation and monitoring of the oxygenation, two dye solutions were formulated to mimic the absorption properties of Hb and HbO_2 at our wavelengths of interest [68, 73-75]. To mimic the absorption of hemoglobin in its oxygenated state, 0.088 % v/v India Ink (Higgins, Black India 44120) and 0.304 mg/mL Epolight 2717^{TM} (Epolin, Inc.) were mixed in a Phosphate Buffered Solution (PBS 0.01M, pH 7.4). The India Ink is used as a baseline because it has an extinction coefficient that covers all of our wavelengths of interest, and the Epolight 2717^{TM} is used to increase the absorption in the NIR region [76, 77]. To mimic the absorbance of hemoglobin in its deoxygenated state, 0.165% v/v India Ink and 2.67% v/v Ink Jet Photo

Cyan (Macro Enter, cat. # FPB085) were mixed in PBS. The absorption coefficients of the two dye solutions compared to that of Hb and HbO_2 along with the output spectrum of the LED source are shown in Figure 6.

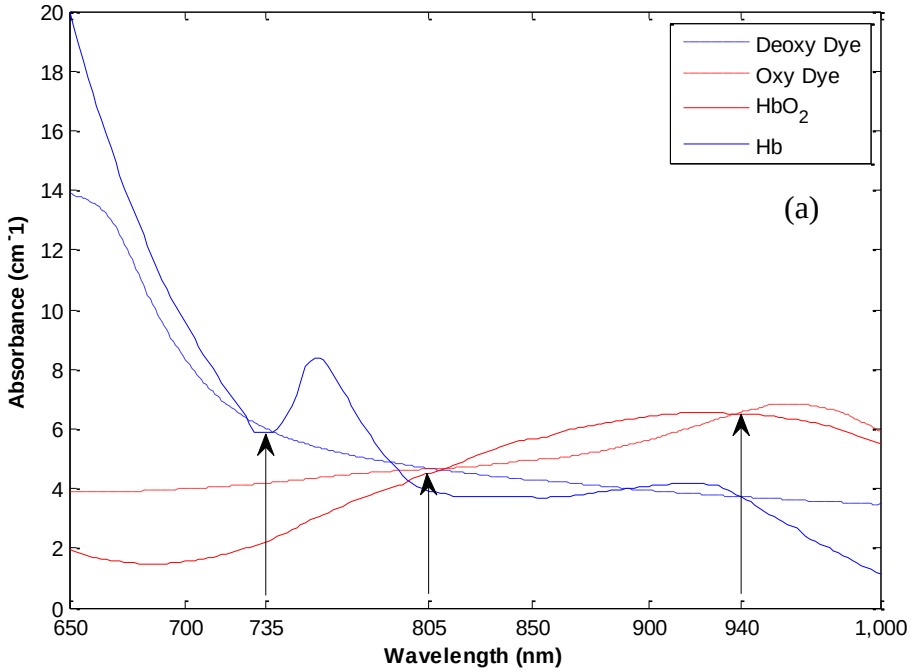

Figure 6: Comparison of the absorption spectrum of HbO_2 (solid red line) and Hb (solid blue line) and the dye solutions mimicking the absorption properties of Hb (dashed blue line) and HbO_2 (dashed red line) (a) and the normalized output power of each wavelength of the LED (b).

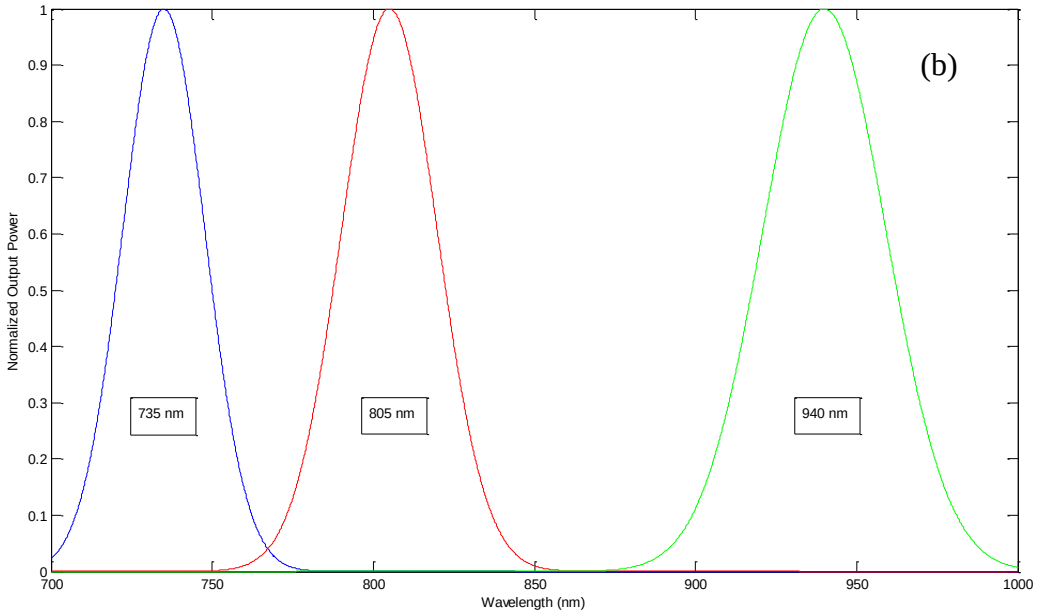

Figure 6: Continued.

To avoid clogging the microfluidic channels of the parenchymal phantoms, the India Ink was filtered through 0.45 µm syringe filters. India Ink was mixed in PBS at a concentration of 0.88% v/v for the oxygenated solution and 1.65% v/v for the deoxygenated solution and filtered through the syringe filters. After the India Ink mixture was filtered through the 0.45 µm syringe filter (VWR, cat. # 28145-481), the absorption spectra of the filtered solutions were measured. After measuring the absorption spectra, Epolight 2717^{TM} and Ink Jet Photo Cyan were then added to the dye solutions mimicking HbO_2 and Hb, respectively.

3.2.3 Flow system setup

To achieve pulsatile flow, which is characteristic of the flow in the liver and the vessels leading to the liver, peristaltic pumps (Gilson, Minipuls 3) were used. To achieve volumetric flow rates in the portal vein phantoms that are within the physiologic range for the portal vein, two peristaltic pumps were used (Figure 7). For the single and multilayer parenchymal phantoms, only one peristaltic pump was used (Figure 8). In both instances, the pumps were driven via a data acquisition board (National Instruments, USB 6009) and a custom program developed using LabVIEW. The driver signal for the peristaltic pumps was a square wave, and the pump frequency and pulse width were set to the desired values to mimic the pulsatile flow pattern of the liver parenchyma and portal vein. For the *in vitro* experiments, the pump frequency was set to 100 pulses per minute to match the *in vivo* porcine data. For the perfusion experiments, the pulse height of the pumps was varied to mimic volumetric flow rate variations within the physiologic range of the liver.

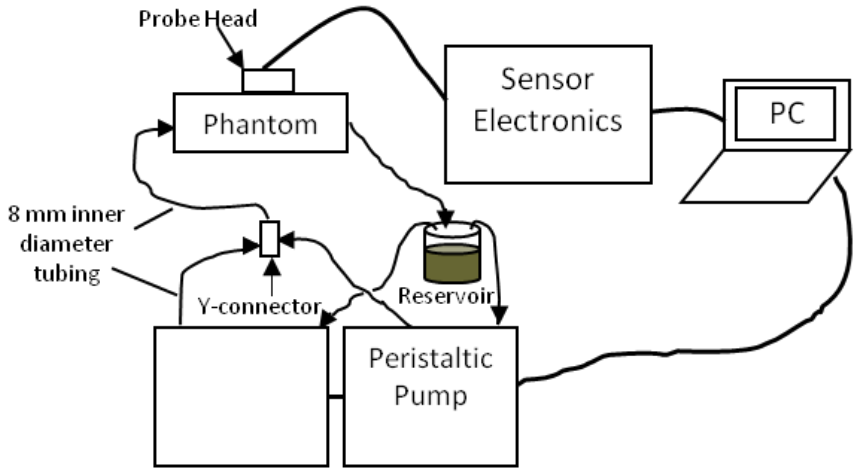

Figure 7: Block diagram of the *in vitro* setup used for the portal vein phantom.

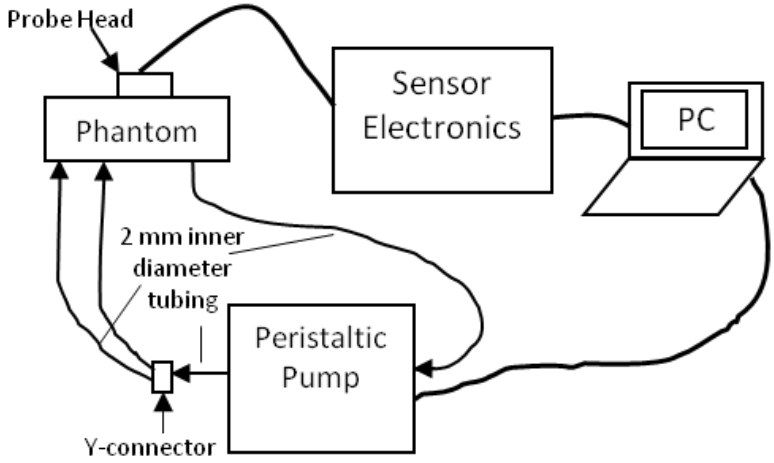

Figure 8: Block diagram of the *in vitro* setup used for the parenchymal phantoms.

Loading of the parenchymal phantoms with the dye solutions required a slight modification of the procedure used for the portal vein phantoms. This modification came in the form of using two syringe pumps to load the phantoms with the dye solutions. The first syringe pump (Harvard Apparatus, cat. # 70-2208) was connected to the input ports

and set to pump at a volumetric flow rate of 0.3 mL/min and 0.9 mL/min for the single and multilayer phantom, respectively, and the second syringe pump (New Era Pump Systems, Inc., NE-4000) was connected to the output ports and set to withdraw at a rate of 0.35 mL/min and 0.95 mL/min for the single and multilayer phantom, respectively. This syringe pump configuration was used to prevent the connections between the needles and the ports from bursting under the pressure of the fluid. The second pump was set to withdraw at a higher volumetric flow rate than the first pump was pumping to establish a negative pressure gradient within the microfluidic channels to further aid in preventing the connections from bursting.

3.2.4 Data collection

In order to assess the ability of the phantoms to mimic the *in vivo* case regarding oxygenation and perfusion, two sets of experiments were performed. The first set of experiments involved pulsing a dye solution mimicking the absorption properties of 100% oxygenated hemoglobin through each of the phantoms and varying the volumetric flow rate of the dye solutions. The second set of experiments involved keeping the perfusion constant while varying the concentrations of the dyes to mimic different oxygenation states of blood. Dyes mimicking 0%, 30%, and 50-100% oxygenation were pulsed through the parenchymal phantoms.

In vivo data was collected from the portal vein and liver parenchyma of female swine to determine the effectiveness of the phantoms to mimic the physiologic flow properties of actual portal vein and liver parenchyma. The data was collected from

probes placed on the female swine's liver parenchyma and portal vein. This procedure was performed under an approved protocol and will be further described in Section 3.3.

To assess optical coupling of the phantom, initial perfusion experiments on the single layer parenchymal phantom were conducted with and without the use of optical coupling gel. A small amount of optical coupling gel (Thorlabs; part # G608N) was placed on the surface of the 3-LED light source and on the silicon photodetector to eliminate any air gaps present between the LED surface, silicon photodtector surface, and the phantom surface. The same procedure was performed for the multilayer parenchymal phantom.

To assess the effect of material compliance, experiments were conducted on the portal vein phantom containing a rigid plastic tube in the center and on the portal vein phantom consisting of a hollow tube through the center. The pulse rate of the peristaltic pump was set at 100 pulses per minute, and the AC and DC signals were acquired with the sensor system. A Fast Fourier Transform (FFT) was performed on the AC signals acquired from both phantoms, and the FFT peak presence, location, and height were evaluated. For each experiment, the same setup described in Section 3.2.3 was used.

3.3 *In vivo* system setup

3.3.1 In vivo *occlusion studies*

For approximately 15 minutes prior to induction with anesthesia a female swine was premedicated with Telazol (5-10 mg/kg) and Buprenorphine (0.01-0.05 mg/kg) intramuscularly (IM). Anesthesia was induced by administering isoflurane (~3-4%) in oxygen at a rate of 3L/min via a face mask. An appropriately sized endotracheal tube

was used to intubate the swine according to the approved animal use protocol. Maintenance of anesthesia was achieved with Isoflurane (0.5-4%) in Oxygen (15 mL/lb, maximum 5L). The swine's SpO_2 was monitored by a pulse oximetry probe placed on the swine's ear. To allow venous access, a catheter (~18-20 g) was inserted and secured in the auricular vein. Mechanical respiration was provided at a rate of 8-12 breaths per minute (BPM) and tidal volume of 5-10 mL/lb via a ventilator.

A laparotomy was performed to gain access to the liver parenchyma, portal vein, and hepatic artery, and the custom prototype probes were stitched onto the left and right lobe of the liver, on the hepatic artery, and on the portal vein. Mechanical vessel occluders were secured around the hepatic artery and portal vein to perform the vessel occlusion studies. Before occlusion of each vessel, at least one 60 second segment of data was collected to establish a baseline. The data set for the *in vivo* study consisted of 24, 60 second segments. Each segment was analyzed using FFT analysis.

CHAPTER IV

RESULTS AND DISCUSSION

The first section of this chapter presents the results of a compliance assessment performed on the portal vein phantoms. The second section of this chapter presents a study performed on the coupling effectiveness of the PDMS-based phantoms. The next section of this chapter contains a comparison of the *in vitro* data gathered from perfusion studies on the phantoms to *in vivo* data collected while performing vascular occlusion studies on a female swine. The final section of this chapter presents oxygenation studies performed on the phantoms.

4.1 Phantom compliance

Figure 9 displays a 10-second segment of the time-domain AC signal measured with the noncompliant (a) portal vein phantom along with the corresponding Fast Fourier Transform (FFT) of the entire 60-second data segment (b) in comparison to a 10-second segment of the time-domain AC signal measured with the compliant portal vein phantom (c) and the corresponding FFT of the 60-second data segment (d). Also pictured is a 10-second segment of the time-domain AC signal taken from the porcine portal vein (e) and the corresponding FFT of the complete 60-second data set (f). For each *in vitro* experiment, the probe LED and photodetector were placed directly on top of the phantom and in line with the tube that allowed the dye solutions to be pulsed through the phantoms.

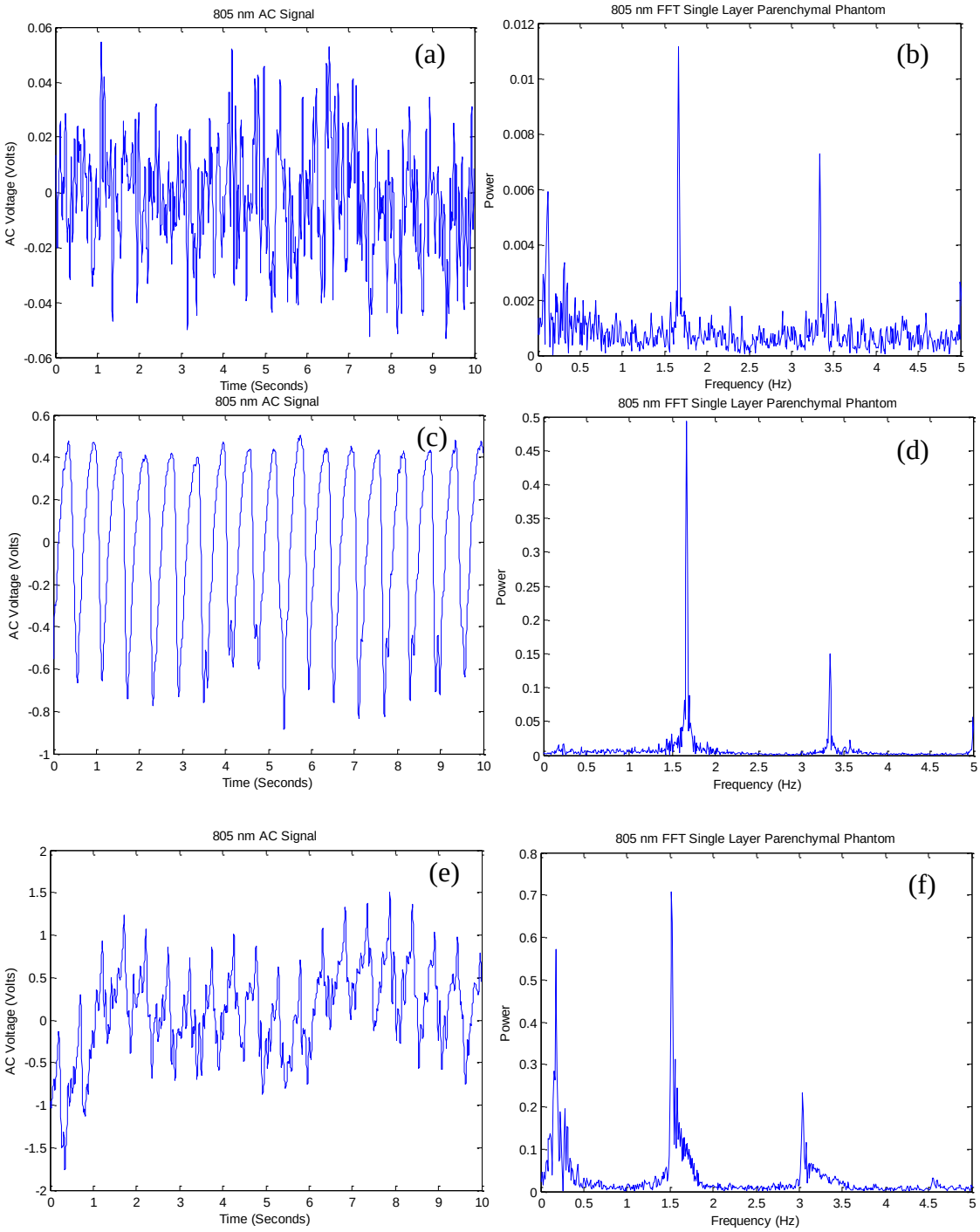

Figure 9: 10-second data segments of the time-domain AC signal measured on the non-compliant (a) and compliant (c) portal vein phantoms as well as the pig portal vein (e) along with the corresponding FFT spectra of 60-second data segments of the time-domain AC signal gathered with the non-compliant (b) and compliant (d) portal vein phantoms as well as the pig portal vein (f).

The non-compliant phantom was incapable of producing an AC signal, as was expected due to the presence of a rigid (non-compliant) tube through the center of the phantom. The FFT spectrum of the data gathered from the non-compliant phantom shows a peak at the frequency (1.667Hz) that corresponds to the pump pulse rate (100 bpm). However, with the compliant portal vein phantom, an AC signal was produced resulting in an FFT spectrum containing a peak at 1.667 Hz that was an order of magnitude higher than the peak at 1.667 Hz measured with the non-compliant portal vein phantom. Also, the time-domain AC signal of the compliant portal vein phantom more closely mimics the time-domain AC signal of the *in vivo* data set (Figure 9e, 9f). As a result of this observation, ensuing *in vitro* experiments regarding the portal vein were performed on the compliant portal vein phantom. Note that the ratio of the second harmonic peak to the first harmonic peak in the FFT spectrum of data taken from the non-compliant phantom is larger than the ratio of the second harmonic peak to the first harmonic peak in the FFT spectrum of data taken from the compliant phantom and from the actual portal vein of the pig. The ratio of the second harmonic peak to the first harmonic peak is lowest in the FFT spectrum of the actual portal vein data. Further studies must be done to determine if this ratio is a function of the compliance of the vessel.

4.2 Optical coupling

To maximize the signal measured by the sensor system, it is important to maximize the amount of light that reaches the photodetector or minimize the amount of light lost at the interface of the photodetector and phantom surface due to the difference

in the index of refraction of the glass coating the photodetector (n = 1.4), air (n = 1.33), and PDMS (wavelength dependent; n_{735} = 1.4089, n_{805} = 1.4076, and n_{940} = 1.4056). Experiments on the single layer parenchymal phantom were performed with and without coating the surface of the sensor with optical coupling gel for comparison. Figure 10 displays a comparison of the FFT of the time-domain AC signals measured with (a) and without (b) the use of optical coupling gel.

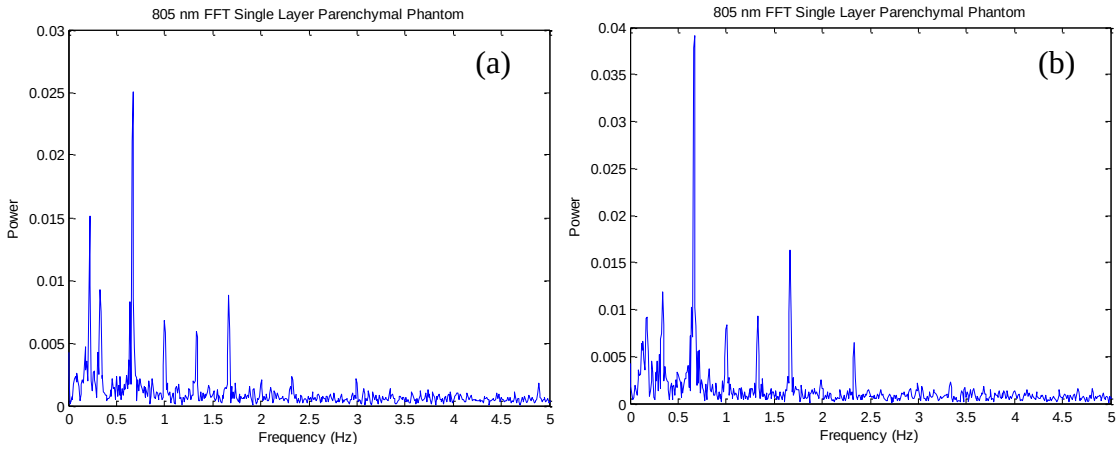

Figure 10: 10-second segment of the time domain AC signal measured from the single layer parenchymal phantom without (a) and with (b) optical coupling gel.

It can be seen that with the use of optical coupling gel, the magnitude of the peak in the FFT spectrum at 1.67 Hz is greater than the magnitude of the peak in the FFT spectrum of the signal collected without the use of optical coupling gel. Also, the DC voltages measured by the sensor system from light collected from experiments run with the use of optical coupling gel is slightly higher than the DC voltages measured without

the use of optical coupling gel (Table 1), indicating that more light is collected by the photodetector. As a result of this observation, optical coupling gel was used for all *in vitro* perfusion and oxygenation experiments.

Table 1: DC voltages measured with and without the use of optical coupling gel.

Wavelength	735 nm	805 nm	940 nm
Single Layer Parenchymal Phantom			
DC signal: No optical coupling gel	1.249 V	1.914 V	1.181 V
DC signal: Optical coupling gel	1.699 V	2.565 V	1.622 V
Compliant Portal Vein Phantom			
DC signal: No optical coupling gel	1.174 V	1.75 V	1.333 V
DC signal: Optical coupling gel	1.397 V	2.083 V	1.602 V

4.3 Perfusion studies

To assess how well the phantoms mimicked the flow properties of liver parenchyma and of the portal vein, perfusion studies were performed on the single layer, multilayer, and portal vein phantoms, and the data collected was compared to *in vivo* data collected from vessel occlusion studies performed on female swine. For the single and multilayer phantoms, the comparison was performed to assess the ability of the phantoms to mimic the physiologic response of perfused liver parenchyma.

4.3.1 In vitro *perfusion studies*

To simulate a decrease in perfusion of blood entering the liver parenchyma, the peristaltic pump was set to pump at different levels that corresponded to a specific volumetric flow rate of the dye solutions. As blood enters the liver parenchyma, light at our wavelengths of interst (735, 805, and 940 nm) is absorbed by the hemoglobin present in the blood. While the absorption coefficients at the 735 nm and 940 nm wavelengths vary with oxygenation, the absorption at all three wavelengths varies with perfusion (assuming oxygenation is held constant). Higher levels of perfusion result in an increase in the amount of blood being pulsed through the vessels and organs. As more blood is pulsed through the volume of tissue, the difference in the amount of blood present during systole and diastole is greater and translates into more light being absorbed with each pulse. Therefore, an increase or decrease in perfusion should result in an increase or decrease in the absorption, respectively, at each of the three wavelengths. This increase or decrease in absorption can be observed as an increase or decrease, respectively, in the amplitude of the time-domain AC signal and can be observed in the corresponding FFT of the AC signal. Figure 11 displays 10-second segments of the time domain AC signals measured from the single layer (Figure 11a) and multilayer (Figure 11c) parenchymal phantoms along with the FFT of the entire 60-second data segment. Figure 12 displays a 10-second segment of the time domain AC signal measured from porcine liver parenchyma along with the corresponding FFT of the entire 60 second data segment. The AC/DC ratio is slightly higher for the multilayer phantom, which is expected because the multilayer phantom contains more lobules and

is capable of storing a larger volume of dye solution. This increased volume results in a larger AC signal measured from the pulsatile flow induced by the peristaltic pumps. However, this increased AC signal comes at the expense of less homogeneous waveform which is most likely due to the presence of three layers of lobules.

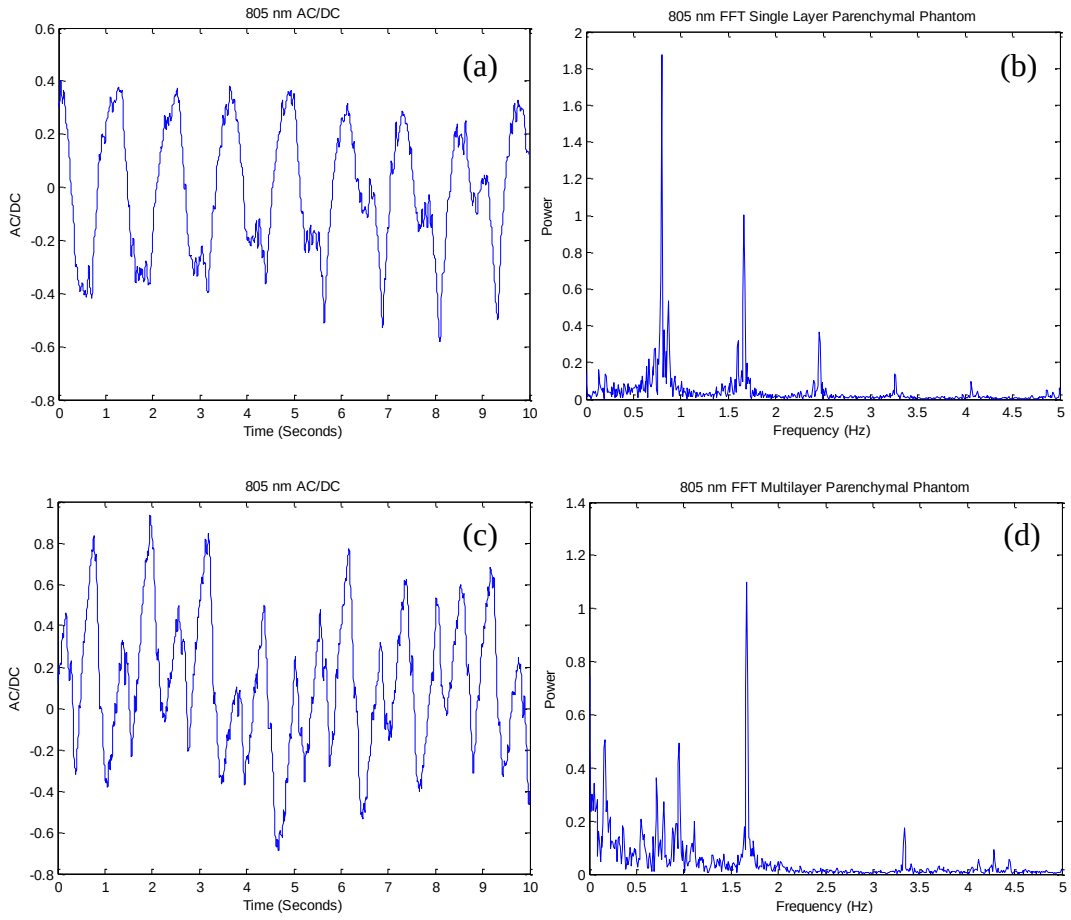

Figure 11: 10-second segment of the time-domain AC signal measured from the single layer (a) and multilayer (c) parenchymal phantoms along with the corresponding FFT spectrum of a 60 second segment of data measured from the single layer (b) and multilayer (d) parenchymal phantoms.

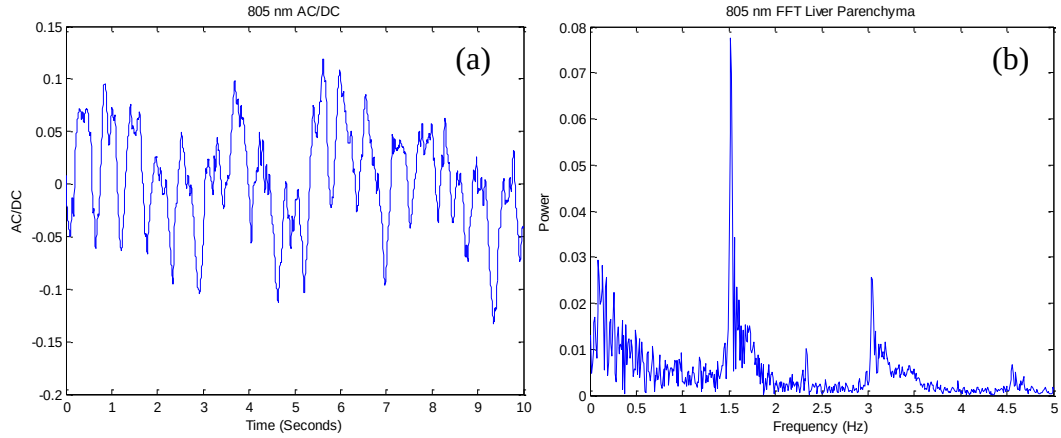

Figure 12: 10 second segment of the time-domain AC signal measured from porcine liver parenchyma (a) along with the FFT of the entire 60 second data segment (b).

Figure 13 displays the normalized values of the FFT peak at 1.667 Hz at each wavelength vs. perfusion for the single layer parenchymal phantom. At each wavelength, the FFT peak value decreases linearly with a decrease in perfusion of the dye solutions. To assess the sensitivity of the phantoms to changes in perfusion, a linear fit was applied to the data. For the single layer parenchymal phantom, the slope of the fit at 735 nm, 805 nm, and 940 nm is 1.07; 1.08; and 1.09, respectively. This observation indicates that the absorption at each wavelength increases at approximately the same rate, as is expected because the volume per pulse and not the oxygen saturation was altered.

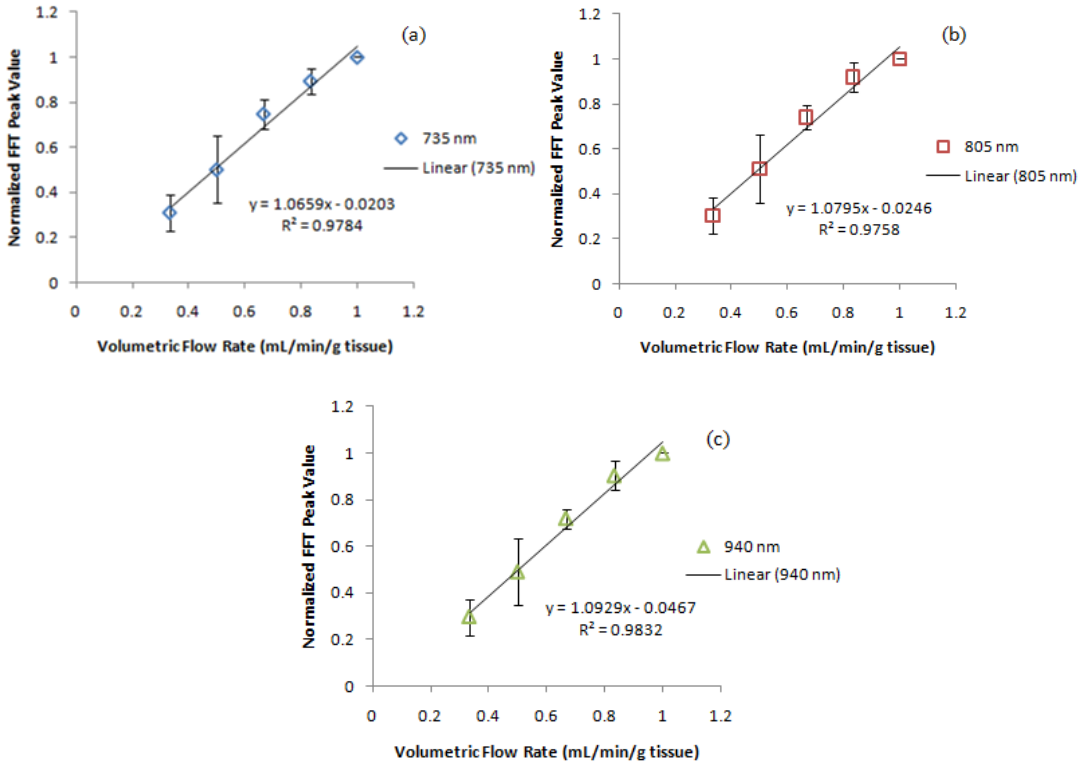

Figure 13: Signal measured at 735 nm (a), 805 nm (b), and 940 nm (c) from *in vitro* perfusion experiments on the single layer parenchymal phantom.

Figure 14 displays the normalized values of the FFT peak at 1.667 Hz at each wavelength vs. perfusion for the multi-layer parenchymal phantom. As with the single layer parenchymal phantom, the FFT peak values at each wavelength decrease linearly with a decrease in perfusion. The slope of the linear fit for the 735 nm, 805 nm, and 940 nm wavelengths is 1.41; 1.36; and 1.34, respectively, indicating that the absorption at each wavelength is increasing at the same rate with an increase in perfusion. This same observation is true for the single layer parenchymal phantom. However, the slope of the linear fit at each wavelength is approximately 30% higher in the multilayer phantom,

indicating a higher sensitivity to changes in perfusion with the data collected from the multilayer phantom.

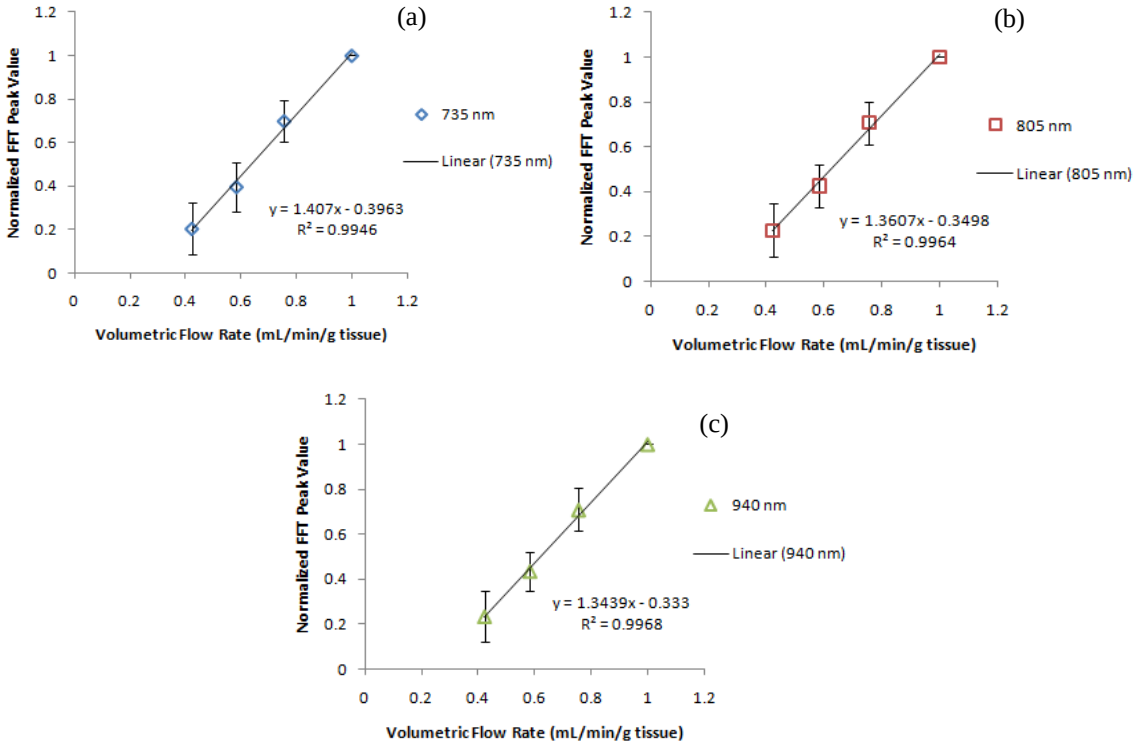

Figure 14: Signal measured at 735 nm (a), 805 nm (b), and 940 nm (c) from *in vitro* perfusion experiments on the multilayer parenchymal phantom.

As predicted, with a decrease in perfusion, the FFT peak value decreases at each of the three wavelengths indicating the presence of less dye solution being pulsed through the parenchymal phantoms. Under the same volumetric flow rates per gram of tissue, the slope of the data taken from perfusion studies on the multilayer phantom is

greater than that of the single layer phantom indicating a higher sensitivity to changes in perfusion and a greater resolution for the sensor. The higher sensitivity in the multilayer phantom is expected due to the presence of a higher total volume of dye solution per pulse resulting from more lobules being present in the multilayer phantom (1200 lobules) than in the single layer phantom (400 lobules). This higher volume of dye solution results in a better signal (AC/DC; see Figure 11) being extracted from the perfusion data. However, although the slopes of the linear fits are roughly the same, the values contain slight differences at the different wavelengths for both phantoms. For example, the slope of the linear fit for the 735 nm wavelength is less than the slope of the linear fit for the 940 nm wavelength for the single layer parenchymal phantom (Figure 13). This small difference in the slopes may produce errors in S_aO_2 values due to perfusion. Theoretically, a change in perfusion should not produce a change in the measured S_aO_2, but this difference in slopes at the different wavelengths could result in an S_aO_2 value that decreases with a change in perfusion. While this observation is not a problem for experiments limited to perfusion only, when attempting to simultaneously measure perfusion and oxygen saturation, the change in S_aO_2 with perfusion will cause a problem. The same problem exists with data gathered from the multi-layer phantom. However, an opposite effect could be produced resulting in an S_aO_2 that increases with an increase in perfusion due to the greater slope at the 735 nm wavelength than the 940 nm wavelength (Figure 14). Figure 15 displays the values of R (Equation 1) vs. perfusion. The R value decreases with an increase in perfusion in the single layer phantom, which corresponds to an increase in the measured S_aO_2 as perfusion increases.

However, the R value increases with an increase in perfusion in the multi-layer phantom, which corresponds to a decrease in the measured S_aO_2 as perfusion increases. While opposite effects were produced with each phantom, the same problem exists. Changes in the measured R value indicate changes in S_aO_2, and this effect would lead to erroneous S_aO_2 measurements in the presence of stable oxygenation with changing perfusion.

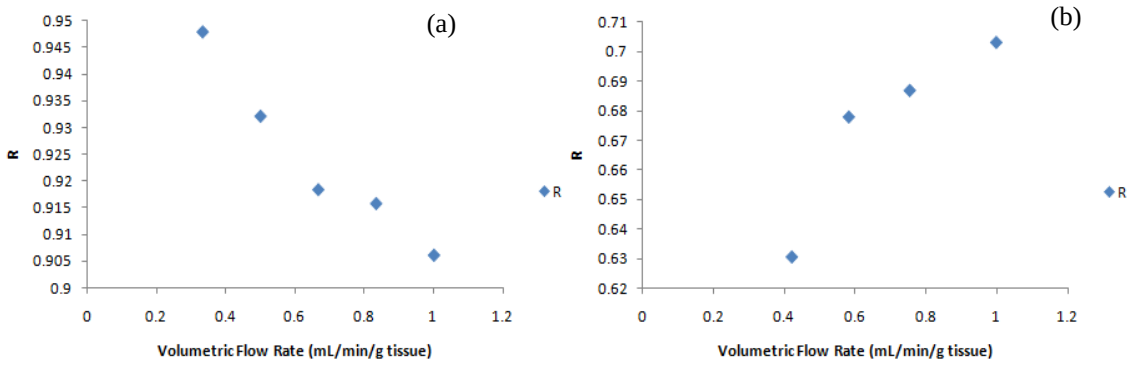

Figure 15: R vs. perfusion for *in vitro* perfusion experiments performed on the single layer (a) and multi-layer (b) parenchymal phantoms.

The data gathered from perfusion studies performed on the compliant portal vein phantom displays similar trends to the data gathered from perfusion studies performed on the parenchymal phantoms (Figure 16). As with the parenchymal phantoms, the FFT peak value increases with a increase in perfusion. The FFT peak value increases at the same rate for each of the wavelengths, which is expected due to the change in perfusion with constant oxygen saturation.

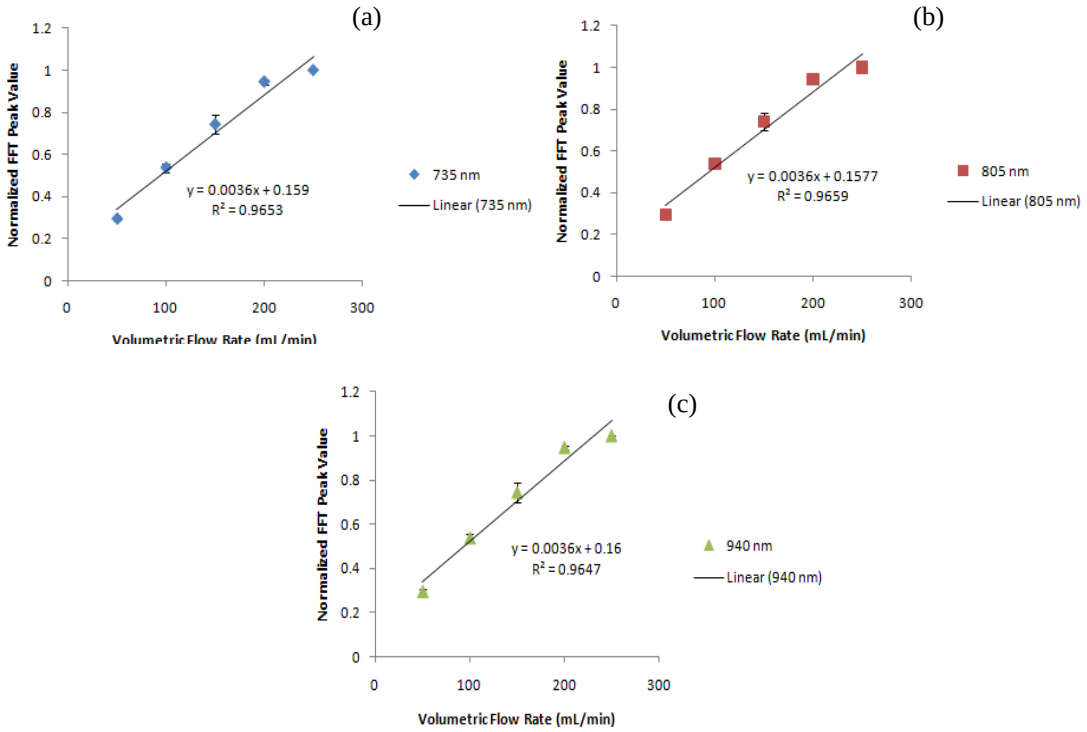

Figure 16: Signal measured at 735 nm (a), 805 nm (b), and 940 nm (c) from *in vitro* perfusion experiments on the compliant portal vein phantom.

4.4 Occlusion studies

To assess the ability of both phantoms to mimic liver parenchyma physiologically, in vitro occlusion studies were performed to evaluate and compare the response of the phantoms in the presence of a blockage in flow to in vivo results collected from occlusion studies on a pig liver parenchyma. In each phantom, a simulation of 50% and 100% blockage of flow were created by decreasing the volumetric flow rates of the peristaltic pumps by 50% and 100%, respectively. For the *in vivo* occlusion study, a total occlusion was created by the use of mechanical occluders on both the portal vein and hepatic artery.

4.4.1 In vitro *occlusion studies*

Figure 17 displays the results of the *in vitro* occlusion studies on the single layer (Figure 17a) and multilayer (Figure 17b) parenchymal phantoms. During 50% occlusion, the signal measured from both phantoms at each wavelength decreases to approximately 50% of the baseline values. This observation is consistent with the 50% decrease in the volumetric flow rate from the peristaltic pump. Also, during total occlusion, the signal at each wavelength measured from both phantoms decreases to zero, consistent with the 100% decrease in flow from the peristaltic pump. The remaining data points indicate the ability of both phantoms to recover during fully restored flow. All simulations were performed with the dye solution mimicking the absorption properties of HbO_2, which explains the greater signal for the 940 nm wavelength. Also, the signal measured from the multilayer phantom is approximately 3 times greater than the signal measured from the single layer phantom, which is consistent with the multilayer phantom containing three times as many layers of lobules than the single layer phantom.

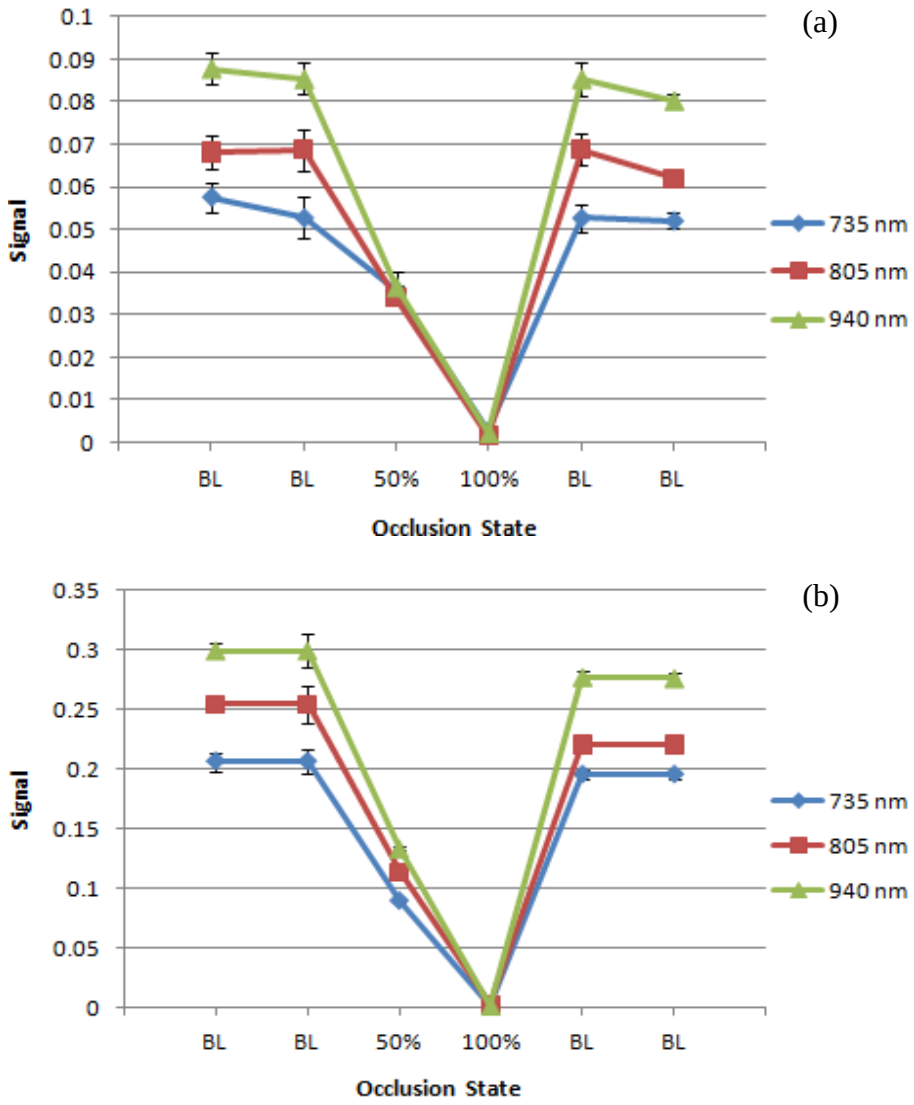

Figure 17: AC/DC measured during *in vitro* occlusion studies performed on the single layer parenchymal phantom (a) and multi-layer parenchymal phantom (b). The results show a decrease in perfusion during simulations of 50% and 100% occlusion of the inputs to the phantoms and an increase as the flow is restored.

4.4.2 In vivo *occlusion studies*

Figure 18 displays the results from the *in vivo* occlusion studies. During 100% occlusion, the signal decreases to nearly zero. This significant decrease is consistent with the significant decrease in flow induced by mechanical occlusion of the vessels. The final data point indicates that the signal recovered to baseline after flow was restored.

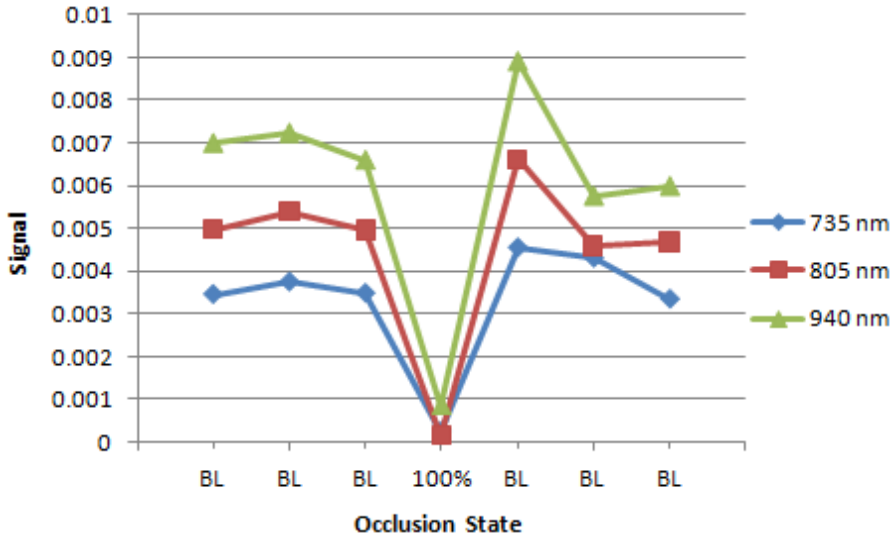

Figure 18: AC/DC signal measured during *in vivo* occlusion studies showing a decrease in signal during full occlusion and an increase in signal as flow is restored.

4.5 Oxygenation studies

In vitro oxygenation studies were performed to determine if the sensor and phantoms could be used for future oxygenation studies. Varying dye solutions mimicking the absorption properties of different hemoglobin oxygen saturations were pulsed through the phantoms at a constant volumetric flow rate. It is expected that as the

oxygen saturation increases, the ratio of absorbance at 735 nm to absorbance at 940 nm will decrease as a result of more oxygenated hemoglobin being present in a specific volume of blood. The presence of more oxygenated hemoglobin results in more 940 nm wavelength light being absorbed. Figure 5 displays the ratio, R, versus the oxygen saturation for the single layer parenchymal phantom. R decreases as oxygen saturation increases for the single layer parenchymal phantom as well as the multilayer parenchymal phantom (Figures 19 and 20). The slopes of the linear fit for the oxygen saturations 60% and above on both phantoms are identical, indicating that the number of sinusoid layers does not affect the R values measured during the oxygenation studies.

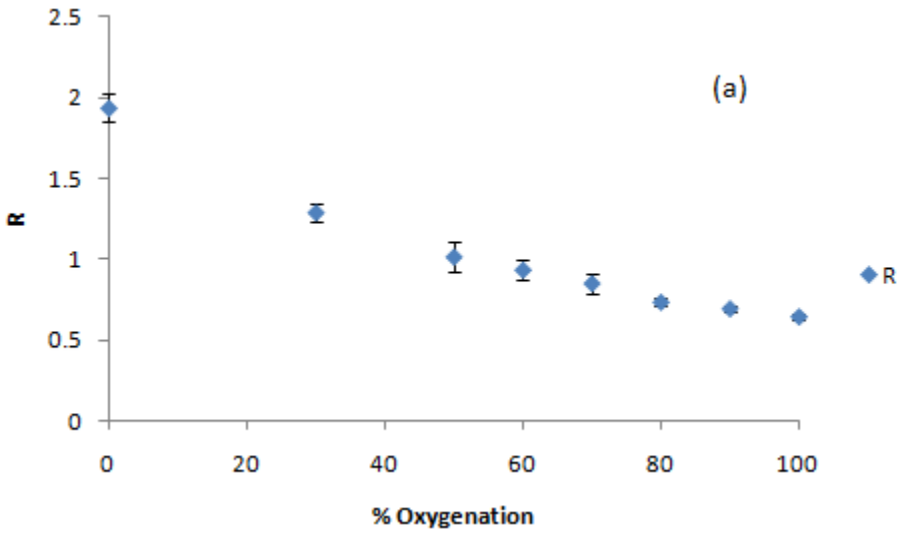

Figure 19: Ratio, R, vs. oxygen saturation for the single layer parenchymal phantom (a) and a cutout showing the data from 60-100% oxygenation (b).

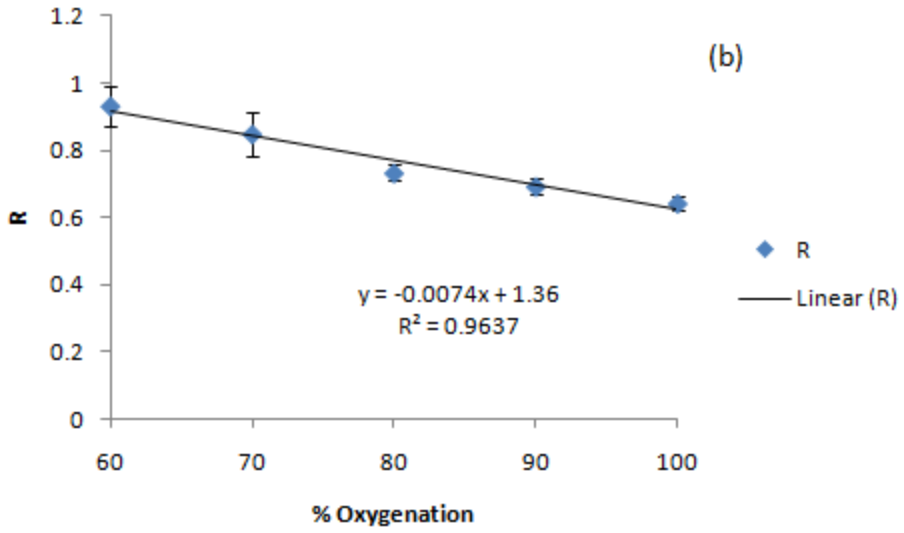

Figure 19: Continued.

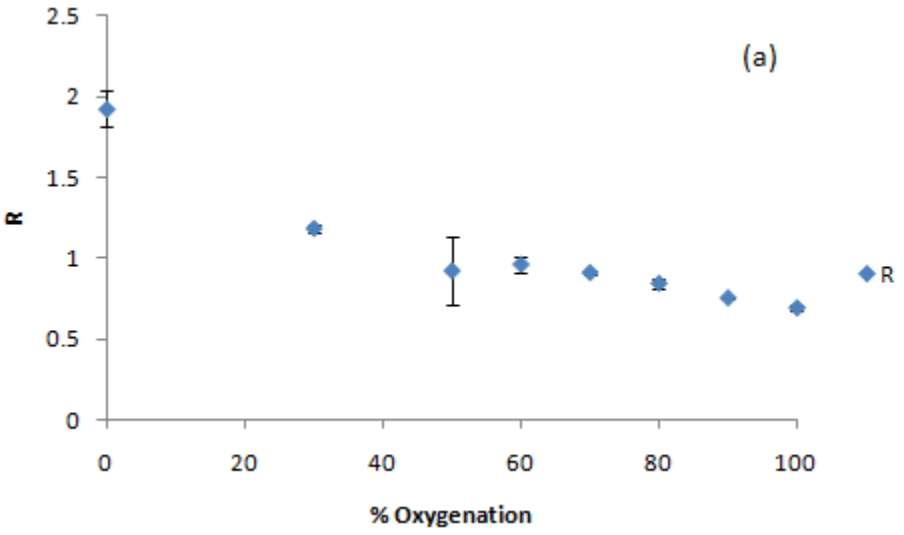

Figure 20: Ratio, R, vs. oxygen saturation for the multilayer parenchymal phantom (a) and a cutout showing the data from 60-100% oxygenation (b).

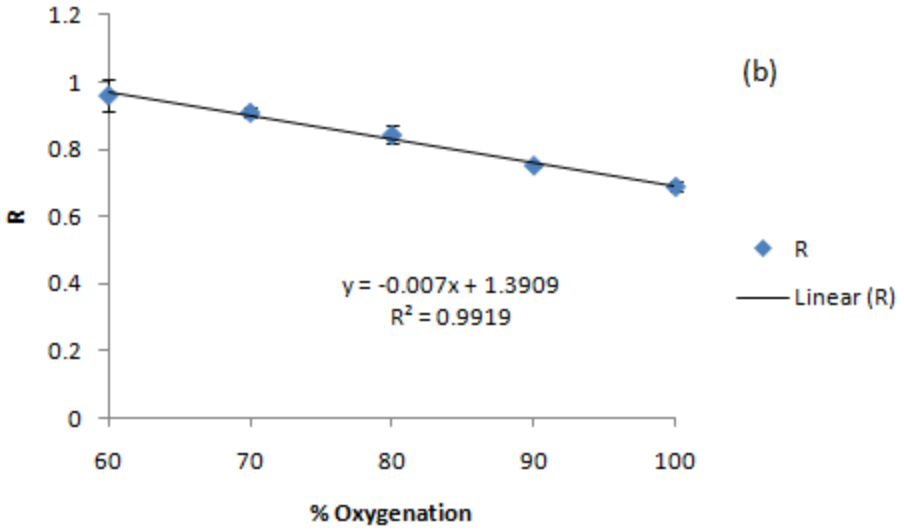

Figure 20: Continued.

It was noted earlier that the R value changes in response to a change in perfusion (Figure 15). While the range of R values over the change in perfusion is relatively small (in comparison to measured R values for traditional pulse oximeters), this range could prove problematic when calibrating the sensor in an attempt to simultaneously measure perfusion and oxygenation *in vitro* due to the small range of R values measured from the *in vitro* oxygenation experiments. For instance, the range of R values of Figure 15 is 0.042 and 0.072 for the single and multi-layer phantoms, respectively. However, the range of R values within the physiologic range of interest (Figure 19b and 20b) for the single and multi-layer parencymal phantoms is 0.291 and 0.271, respectively. The changes in R induced by changes in perfusion represent 15% and 17% of the range of R values for the single layer and multi-layer phantom, respectively. Such a range of R values could lead to erroneous S_aO_2 measurements by the sensor system.

CHAPTER V

CONCLUSIONS AND FUTURE WORK

Phantoms mimicking the optical properties of liver parenchyma have been developed for use with *in vitro* perfusion and oxygenation experiments. Development of such phantoms should aid in facilitating sensor design while reducing the number of animal experiments needed. In this work, data gathered during *in vitro* perfusion and occlusion studies performed on single and multilayer parenchymal phantoms were compared to data gathered from *in vivo* occlusion studies performed on a female swine. Also, the optical coupling to the surface of the PDMS-based phantoms and the compliance of the phantoms were assessed. It was shown that the use of optical coupling gel resulted in more light collected by the photodetector when compared with measurements taken without the use of optical coupling gel. Also, it was shown that by designing a more compliant portal vein phantom with no rigid plastic tube in the center, the system was able to measure a well-defined AC waveform. The ability to measure an AC signal and a peak in the FFT spectrum that corresponded to the pump frequency (1.667 Hz) in both parenchymal phantoms and the portal vein phantom was shown.

In the parenchymal and portal vein phantoms, the FFT peak value decreased as the volumetric flow rate of the dye solutions through the phantoms decreased. Both the single layer and multilayer parenchymal phantoms displayed the same trends in the occlusion studies as the liver parenchyma, but the signal measured with the multilayer phantom was higher than the signal measured with the single layer parenchymal phantom. The signal measured with the multilayer parenchymal phantom was nearly

three times higher than the single layer phantom and showed greater sensitivity to changes in perfusion. These observations demonstrate the ability of the single layer and multilayer phantom to be used for *in vitro* studies to facilitate sensor design. These observations also confirm that it is more applicable to use the multilayer phantom because it more closely mimics the anatomical properties of liver parenchyma but is only slightly more complex in design than the single layer parenchymal phantom. While adding more layers of sinusoids (until the depth of the layers exceeds the penetration depth of the light) should provide an even better response, the addition of more layers will add to the complexity of the phantom due to the number of input and output ports that would be required. Each additional layer would require the addition of three input/output ports or a different design with vertical interconnects between the sinusoid layers could be pursued.

In vitro oxygenation studies were performed on the single layer and multilayer parenchymal phantoms to determine if the phantoms could be used for future oxygenation studies. As the oxygenation increased, the ratio, R, decreased for both phantoms, and showed a similar range of values. Within the physiologic range of interest for oxygenation percentage (60-100% oxygenation), the slopes of the linear fits of both phantoms were identical indicating an identical sensitivity to changes in oxygenation. For future oxygenation studies, it may be more applicable to use the single layer parenchymal phantom because it only has three input ports making it easier to load fluid into and pump fluid through the lobules.

Future work should focus on miniaturization of the sensor system for implantation and redesigning the probe to make it more suitable to attach to the tissue and to vessels during *in vivo* experiments. Studies should be performed to assess the upper and lower limits of detection as well. Also, the compliance of the PDMS should be adjusted to match the compliance of the portal vein and liver parenchyma (where applicable) if possible.

REFERENCES

1. “2009 Annual Report of the U.S. Organ Procurement and Transplantation Network and the Scientific Registry of Transplant Recipients: Transplant Data 1999-2008.” U.S. Department of Health and Human Services, Health Resources and Services Administration, Healthcare Systems Bureau, Division of Transplantation: Rockville, MD.

2. J.P. Duffy, J.C. Hong, D.G. Farmer, R.M. Ghobrial, H. Yersiz, J.R. Hiatt, and R.W. Busuttil, "Vascular complications of orthotopic liver transplantation: experience in more than 4,200 patients." Journal of the American College of Surgeons. **208**(5), 896-903 (2009).

3. T.J. Akl, R. Long, M.J. McShane, M.N. Ericson, M.A. Wilson, and G.L. Coté, "Optimizing probe design for an implantable perfusion and oxygenation sensor." Biomedical Optics Express. **2**(8), 2096-2109 (2011).

4. M.N. Ericson, M.A. Wilson, G. L. Cote, J.S. Baba, W. Xu, M. Bobrek, C. L. Britton, M.S. Hileman, M.R. Moore, M.S. Emery, and R. Lenarduzzi, "Implantable sensor for blood flow monitoring after transplant surgery." Minimally Invasive Therapy and Allied Technologies. **13**(2), 87-94 (2004).

5. M.N. Ericson, M. A. Wilson, G. L. Cote, C.L. Britton, W. Xu, J. S. Baba, M. Bobrek, M. S. Hileman, M. R. Moore, and S. S. Frank, "Development of an implantable oximetry-based organ perfusion sensor," in *Conference Proceedings Engineering in Medicine and Biology Society, 2004* (IEEE, 2004), pp. 2235-2238.

6. H. Subramanian, B.L. Ibey, W. Xu, M.A. Wilson, M.N. Ericson, and G.L. Cote, "Real-time separation of perfusion and oxygenation signals for an implantable sensor using adaptive filtering." IEEE Transactions on Biomedical Engineering. **52**(12), 2016-23 (2005).

7. H. Subramanian, B.L. Ibey, W. Xu, M.A. Wilson, M.N. Ericson, and G.L. Cote, "An autocorrelation-based time domain analysis technique for monitoring perfusion and oxygenation in transplanted organs." IEEE Transactions on Biomedical Engineering. **52**(7), 1355-8 (2005).

8. R. Long, T. King, T. Akl, M.N. Ericson, M. Wilson, G.L. Coté, and M.J. McShane, "Optofluidic phantom mimicking optical properties of porcine livers." Biomedical Optics Express. **2**(7), 1877-1892 (2011).

9. A.C. Guyton, *Textbook of medical physiology*, 8th ed. (Saunders, Philadelphia, 1991). p. 434-440.

10. R.V. Krstić, *Human microscopic anatomy: an atlas for students of medicine and biology*. (Springer-Verlag, Lausanne, Switzerland, 1991). p. 18.

11. T. Aoyagi, "Pulse oximetry: its invention, theory, and future." Journal of Anesthesia. **17**(4), 259-266 (2003).

12. J.G. Webster, *Design of pulse oximeters*. (Taylor and Francis Group, New York City, 1997). p. 194.

13. E.P. Widmaier, H. Raff, and K.T. Strang, *Vander's human physiology: the mechanisms of body function*. (McGraw-Hill Higher Education, New York City, 2008). pp. 478-480; 483-486.

14. N.E. Almond and A.M. Wheatley, "Measurement of hepatic perfusion in rats by laser Doppler flowmetry." American Journal of Physiology. **262**(2 Pt 1), G203-9 (1992).

15. A. Humeau, W. Steenbergen, H. Nilsson, and T. Stromberg, "Laser Doppler perfusion monitoring and imaging: novel approaches." Medical and Biological Engineering and Computing. **45**(5), 421-35 (2007).

16. G.E. Nilsson, T. Tenland, and P.A. Oberg, "Evaluation of a laser Doppler flowmeter for measurement of tissue blood flow." IEEE Transactions on Biomedical Engineering. **27**(10), 597-604 (1980).

17. H.P. Notzli, K.A. Siebenrock, A. Hempfing, L.E. Ramseier, and R. Ganz, "Perfusion of the femoral head during surgical dislocation of the hip: monitoring by laser Doppler flowmetry." Journal of Bone and Joint Surgery - British Volume. **84-B**(2), 300-304 (2002).

18. A.M. Seifalian, S.V. Mallet, K. Rolles, and B.R. Davidson, "Hepatic microcirculation during human orthotopic liver transplantation." British Journal of Surgery. **84**(10), 1391-5 (1997).

19. C. Tziafalia, M. Vlychou, K. Tepetes, N. Kelekis, and I.V. Fezoulidis, "Echo-Doppler measurements of portal vein and hepatic artery in asymptomatic patients with hepatitis B virus and healthy adults." Journal of Gastrointestin Liver Diseases. **15**(4), 343-6 (2006).

20. A.M. Wheatley and D. Zhao, "Intraoperative assessment by laser Doppler flowmetry of hepatic perfusion during orthotopic liver transplantation in the rat." Transplantation. **56**(6), 1315-8 (1993).

21. H.F. Bowman and T.A. Balasubramaniam, "A new technique utilizing thermistor probes for the measurement of thermal properties of biomaterials." Cryobiology. **13**(5), 572-80 (1976).

22. M.B. Khot, P.K. Maitz, B.R. Phillips, H.F. Bowman, J.J. Pribaz, and D.P. Orgill, "Thermal diffusion probe analysis of perfusion changes in vascular occlusions of rabbit pedicle flaps." Plastic Reconstruction Surgery. **115**(4), 1103-9 (2005).

23. E. Klar, T. Kraus, J. Bleyl, W.H. Newman, H.F. Bowman, W.J. Hofmann, R. Kummer, M. Bredt, and C. Herfarth, "Thermodiffusion for continuous quantification of hepatic microcirculation--validation and potential in liver transplantation." Microvascular Research. **58**(2), 156-66 (1999).

24. G.T. Martin and H.F. Bowman, "Validation of real-time continuous perfusion measurement." Medical and Biological Engineering and Computing. **38**(3), 319-25 (2000).

25. P. Vajkoczy, H. Roth, P. Horn, T. Lucke, C. Thomé, U. Hubner, G.T. Martin, C. Zappletal, E. Klar, L. Schilling, and P. Schmiedek, "Continuous monitoring of regional cerebral blood flow: experimental and clinical validation of a novel thermal diffusion microprobe." Journal of Neurosurgery. **93**(2), 265-274 (2000).

26. J.W. Valvano, J.T. Allen, and H.F. Bowman, "The simultaneous measurement of thermal conductivity, thermal diffusivity, and perfusion in small volumes of tissue." Journal of Biomechanical Engineering. **106**(3), 192-7 (1984).

27. D.Y. Yuan, J.W. Valvano, and G.T. Anderson, "Measurement of thermal conductivity, thermal diffusivity, and perfusion." Biomedical Sciences Instrumentation. **29**, 435-42 (1993).

28. M.J. Blomley, R. Coulden, P. Dawson, M. Kormano, P. Donlan, C. Bufkin, and M.J. Lipton, "Liver perfusion studied with ultrafast CT." Journal of Computer Assisted Tomography. **19**(3), 424-33 (1995).

29. B.E. Van Beers, I. Leconte, R. Materne, A.M. Smith, J. Jamart, and Y. Horsmans, "Hepatic perfusion parameters in chronic liver disease: dynamic CT measurements correlated with disease severity." AJR American Journal of Roentgenology. **176**(3), 667-73 (2001).

30. D.A. Boas and A.G. Yodh, "Spatially varying dynamical properties of turbid media probed with diffusing temporal light correlation." Journal of the Optical Society of America A. **14**(1), 192-215 (1997).

31. C. Cheung, J.P. Culver, K. Takahashi, J.H. Greenberg, and A.G. Yodh, "*In vivo* cerebrovascular measurement combining diffuse near-infrared absorption and correlation spectroscopies." Physics in Medicine and Biology. **46**(8) 2053-65 (2001).

32. T. Durduran, R. Choe, G. Yu, C. Zhou, J.C. Tchou, B.J. Czerniecki, and A.G. Yodh, "Diffuse optical measurement of blood flow in breast tumors." Optics Letters. **30**(21) 2915-17 (2005).

33. A.H. Hielscher, A.Y. Bluestone, G.S. Abdoulaev, A.D. Klose, J. Lasker, M. Stewart, U. Netz, and J. Beuthan, "Near-infrared diffuse optical tomography." Disease Markers. **18**(5-6) 313-37 (2002).

34. Y. Shang, Y. Zhao, R. Cheng, L. Dong, D. Irwin, and G. Yu, "Portable optical tissue flow oximeter based on diffuse correlation spectroscopy." Optics Letters. **34**(22) 3556-8 (2009).

35. G. Yu, T. Durduran, G. Lech, C. Zhou, B. Chance, E.R. Mohler, and A.G. Yodh, "Time-dependent blood flow and oxygenation in human skeletal muscles measured with noninvasive near-infrared diffuse optical spectroscopies." Journal of Biomedical Optics. **10**(2) 024027 (2005).

36. G. Yu, T.F. Floyd, T. Durduran, C. Zhou, J. Wang, J.A. Detre, and A.G. Yodh, "Validation of diffuse correlation spectroscopy for muscle blood flow with concurrent arterial spin labeled perfusion MRI." Optics Express. **15**(3) 1064-75 (2007).

37. C. Zhou, S.A. Eucker, T. Durduran, G. Yu, J. Ralston, S.H. Friess, R.N. Ichord, S.S. Margulies, and A.G. Yodh, "Diffuse optical monitoring of hemodynamic changes in piglet brain with closed head injury." Journal of Biomedical Optics. **14**(3) 034015 (2009).

38. A.J. Aschoff, E.M. Merkle, V. Wong, Q. Zhang, M.M. Mendez, J.L. Duerk, and J.S. Lewin, "How does alteration of hepatic blood flow affect liver perfusion and radiofrequency-induced thermal lesion size in rabbit liver?" Journal of Magnetic Resonance Imaging. **13**(1) 57-63 (2001).

39. C.M. Carpenter, R. Rakow-Penner, S. Jiang, B.W. Pogue, G.H. Glover, and K.D. Paulsen, "Monitoring of hemodynamic changes induced in the healthy breast through inspired gas stimuli with MR-guided diffuse optical imaging." American Association of Physicists in Medicine. **37**(4) 1638-46 (2010).

40. J.J. Totman, R. L. O'Gorman, P.A. Kane, and J.B. Karani, "Comparison of the hepatic perfusion index measured with gadolinium-enhanced volumetric MRI in controls and in patients with colorectal cancer." British Journal of Radiology. **78**(926) 105-9 (2005).

41. A. El-Desoky, A.M. Seifalian, M. Cope, D.T. Delpy, and B.R. Davidson, "Experimental study of liver dysfunction evaluated by direct indocyanine green clearance using near infrared spectroscopy." British Journal of Surgery. **86**(8) 1005-1011 (1999).

42. L.R. Jiao, A.A. El-Desoky, A.M. Seifalian, N. Habib, and B.R. Davidson, "Effect of liver blood flow and function on hepatic indocyanine green clearance measured directly in a cirrhotic animal model." British Journal of Surgery. **87**(5) 568-574 (2000).

43. S. Kimura, T. Yoshioka, M. Shibuya, T. Sakano, R. Tanaka, and S. Matsuyama, "Indocyanine green elimination rate detects hepatocellular dysfunction early in septic shock and correlates with survival." Critical Care Medicine. **29**(6) 1159-63 (2001).

44. R.E. Stauber, D. Wagner, V. Stadlbauer, S. Palma, G. Gurakuqi, D. Kniepeiss, F. Iberer, K.H. Smolle, J. Haas, and M. Trauner, "Evaluation of indocyanine green clearance and model for end-stage liver disease for estimation of short-term prognosis in decompensated cirrhosis." Liver International, **29**(10) 1516-20 (2009).

45. H.A. Wynne, L.H. Cope, E. Mutch, M.D. Rawlins, K.W. Woodhouse, and O.P.W. James, "The Effect of Age upon Liver Volume and Apparent Liver Blood flow in Healthy Man." Hepatology. **9**(2) 297-301 (1989).

46. P. Vajkoczy, H. Roth, P. Horn, T. Lucke, C. Thomé, U. Hubner, G.T. Martin, C. Zappletal, E. Klar, L. Schilling, and P. Schmiedek, "Continuous monitoring of regional cerebral blood flow: experimental and clinical validation of a novel thermal diffusion microprobe." Journal of Neurosurgery, **93**(2) 265-274 (2000).

47. M.B. Khot, P.K. Maitz, B.R. Phillips, H.F. Bowman, J.J. Pribaz, and D.P. Orgill, "Thermal diffusion probe analysis of perfusion changes in vascular occlusions or rabbit pedicle flaps." Plastic Reconstructive Surgery. **115**(4) 1103-1109 (2005).

48. L.R. Jiao, A.A. El-Desoky, A.M. Seifalian, N. Habib, B.R. Davidson, "Effect of liver blood flow and function on hepatic indocyanine green clearance measured directly in a cirrhotic animal model." British Journal of Surgery. **87**(5) 568-574 (2000).

49. G. Yu, T. Durduran, C. Zhou, T.C. Zhu, J.C. Finlay, T.M. Busch, S.B. Malkowicz, S.M. Hahn, and A.G. Yodh, "Real-time in situ monitoring of human prostate photodynamic therapy with diffuse light." Photochemistry Photobiology. **82**(5) 1279-84 (2006).

50. T. Aoyagi and K. Miyasaka, "Pulse oximetry: its invention, contribution to medicine, and future tasks." Anesthesia and Analgesia. **94**(1 Suppl) S1-3 (2002).

51. S.J. Barker, J. Curry, D. Redford, and S. Morgan, "Measurement of Carboxyhemoglobin and Methemoglobin by Pulse Oximetry: A Human Volunteer Study." Anesthesiology. **105**(5) 892-897 (2006).

52. R.T. Brouillette, A. Morielli, A. Leimanis, K.A. Waters, R. Luciano, and F.M. Ducharme, "Nocturnal Pulse Oximetry as an Abbreviated Testing Modality for Pediatric Obstructive Sleep Apnea." Pediatrics. **105**(2) 405-412 (2000).

53. K.A. Carlson and J.S. Jahr, "A historical overview and update on pulse oximetry." Anesthesiology Review. **20**(5) 173-81 (1993).

54. H.J. Choi, M.S. Little, S.Z. Garber, and K.K. Tremper, "Pulse oximetry for monitoring during ward analgesia: epidural morphine versus parenteral narcotics." Journal of Clinical Monitoring. **5**(2) 87-9 (1989).

55. F. Goffinet, B. Langer, B. Carbonne, N. Berkane, D. Tardif, F. Le Goueff, M. Laville, and F. Maillard, "Multicenter study on the clinical value of fetal pulse oximetry. I. Methodologic evaluation. The French Study Group on Fetal Pulse Oximetry." American Journal of Obstetetrics and Gynecology. **177**(5) 1238-46 (1997).

56. P. Hutton and T. Clutton-Brock, "The benefits and pitfalls of pulse oximetry." British Medical Journal. **307**(6902) 457-8 (1993).

57. A. Jubran, "Pulse oximetry." Critical Care. **3**(2) R11-R17 (1999).

58. Y. Mendelson, "Pulse oximetry: theory and applications for noninvasive monitoring." Clinical Chemistry. **38**(9) 1601-7 (1992).

59. J.T. Moller, N.W. Johannessen, K. Espersen, O. Ravlo, B.D. Pedersen, P.F. Jensen, N.H. Rasmussen, L.S. Rasmussen, T. Pedersen, J.B. Cooper *et al*., "Randomized evaluation of pulse oximetry in 20,802 patients: II. Perioperative events and postoperative complications." Anesthesiology. **78**(3) 445-53 (1993).

60. N. Netzer, A.H. Eliasson, C. Netzer, and D.A. Kristo, "Overnight pulse oximetry for sleep-disordered breathing in adults: a review." Chest. **120**(2) 625-33 (2001).

61. S. Reichelt, J. Fiala, A. Werber, K. Forster, C. Heilmann, R. Klemm, and H. Zappe, "Development of an implantable pulse oximeter." IEEE Transactions on Biomedical Engineering. **55**(2 Pt 1) 581-8 (2008).

62. L.M. Schnapp and N.H. Cohen, "Pulse oximetry. Uses and abuses." Chest. **98**(5) 1244-50 (1990).

63. J.W. Severinghaus, "The history of clinical oxygen monitoring." International Congress Series. **1242** 115-120 (2002).

64. J.W. Severinghaus and J.F. Kelleher, "Recent developments in pulse oximetry." Anesthesiology. **76**(6) 1018-38 (1992).

65. A.J. Williams, G. Yu, S. Santiago, and M. Stein, "Screening for sleep apnea using pulse oximetry and a clinical score." Chest. **100**(3) 631-635 (1991).

66. D.H. Wong, K.K. Tremper, J. Davidson, J. Zaccari, P. Weidoff, S. Wilbur, and E.A. Stemmer, "Pulse Oximetry is Accurate in Patients with Dysrhythmias and a Pulse Deficit." Anesthesiology. **70**(6) 1024 (1989).

67. K.K. Tremper, "Pulse oximetry." Chest. **95**(4) 713-5 (1989).

68. S. Prahl, "Optical Absorption of Hemoglobin." (*www.olmc.org*, 1999), retrieved May 20,2011, *http://omlc.ogi.edu/spectra/hemoglobin/*.

69. K.K. Tremper and S.J. Barker, "Pulse oximetry." Anesthesiology. **70**(1) 98-108 (1989).

70. B. Carbonne, B. Langer, F. Goffinet, F. Audibert, D. Tardif, F. Le Goueff, M. Laville, and F. Maillard, "Multicenter study on the clinical value of fetal pulse oximetry. II. Compared predictive values of pulse oximetry and fetal blood analysis. The French study group on fetal pulse oximetry." American Journal of Obstetetrics and Gynecology. **177**(3) 593-8 (1997).

71. M.T. Petterson, V.L. Begnoche, and J.M. Graybeal, "The effect of motion on pulse oximetry and its clinical significance." Anesthesia and Analgesia. **105**(6 Suppl) S78-84 (2007).

72. A.R. Visram, R.D.M. Jones, M.G. Irwin, and J. Bacon-Shone, "Use of two oximeters to investigate a method of movement artefact rejection using photoplethysmographic signals." British Journal of Anaesthesia. **72**(4) 388-392 (1994).

73. D.J. Faber, M.C. Aalders, E.G. Mik, B.A. Hooper, M.J. van Gemert, and T.G. van Leeuwen, "Oxygen saturation-dependent absorption and scattering of blood." Physics Review Letters. **93**(2) 028102 (2004).

74. M. Friebel, J. Helfmann, U. Netz, and M. Meinke, "Influence of oxygen saturation on the optical scattering properties of human red blood cells in the spectral range 250 to 2,000 nm." Journal of Biomedical Optics. **14**(3) 034001 (2009).

75. A. Roggan, M. Friebel, K. Dörschel, A. Hahn, and G. Müller, "Optical Properties of Circulating Human Blood in the Wavelength Range 400-2500 nm." Journal of Biomedial Optics. **4**(1) 36-46 (1999).

76. P.D. Ninni, F. Martelli, G. Zaccanti, "The use of India Ink in tissue-simulating phantoms." Optics Express. **18**(26) 26854-26865 (2010).

77. S.J. Madsen, M.S. Patterson, and B.C. Wilson, "The use of india ink as an optical absorber in tissue-simulating phantoms." Physics in Medicine and Biology. **37**(4) 985-993 (1992).

APPENDIX A

MATLAB PROGRAM *FFT Program.m*

```
Fs = 300;
T = 1/Fs;
A_735 = A(:,2);
A_805 = A(:,3);
A_940 = A(:,4);
L = length(A(:,1));
L_735 = length(A_735);
L_805 = length(A_805);
L_940 = length(A_940);
t = (0:L-1)*T;
NFFT_735 = 2^nextpow2(L_735);
NFFT_805 = 2^nextpow2(L_805);
NFFT_940 = 2^nextpow2(L_940);
Y_735 = fft(A_735,NFFT_735)/L_735;
Y_805 = fft(A_805,NFFT_805)/L_805;
Y_940 = fft(A_940,NFFT_940)/L_940;
f_735 = Fs/2*linspace(0,1,NFFT_735/2+1);
f_805 = Fs/2*linspace(0,1,NFFT_805/2+1);
f_940 = Fs/2*linspace(0,1,NFFT_940/2+1);

figure; plot(f_735,2*abs(Y_735(1:NFFT_735/2+1))); xlabel('Frequency
(Hz)'); ylabel('Power'); title('735 nm FFT Single Layer Parenchymal
Phantom'); set(gca,'XLim',[0 5]);

figure; plot(f_805,2*abs(Y_805(1:NFFT_805/2+1))); xlabel('Frequency
(Hz)'); ylabel('Power'); title('805 nm FFT Single Layer Parenchymal
Phantom'); set(gca,'XLim',[0 5]);

figure; plot(f_940,2*abs(Y_940(1:NFFT_940/2+1))); xlabel('Frequency
(Hz)'); ylabel('Power'); title('940 nm FFT Single Layer Parenchymal
Phantom'); set(gca,'XLim',[0 5]);

figure; plot(A(1:3000,1),A(1:3000,2)); xlabel('Time (Seconds)');
ylabel('AC Voltage (Volts)'); title('735 nm AC Signal');

figure; plot(A(1:3000,1),A(1:3000,3)); xlabel('Time (Seconds)');
ylabel('AC Voltage (Volts)'); title('805 nm AC Signal');

figure; plot(A(1:3000,1),A(1:3000,4)); xlabel('Time (Seconds)');
ylabel('AC Voltage (Volts)'); title('940 nm AC Signal');

FFT_735 = 2*abs(Y_735(1:NFFT_735/2+1));
FFT_805 = 2*abs(Y_805(1:NFFT_805/2+1));
FFT_940 = 2*abs(Y_940(1:NFFT_940/2+1));
FFT = [FFT_735 FFT_805 FFT_940];
```

```
AC_735 = 2*abs(Y_735(1:NFFT_735/2+1));
AC_805 = 2*abs(Y_805(1:NFFT_805/2+1));
AC_940 = 2*abs(Y_940(1:NFFT_940/2+1));

AC = [AC_735(183,1) AC_805(183,1) AC_940(183,1)];
DC = [mean(A(:,5)) mean(A(:,6)) mean(A(:,7))];

%%%%%%%%%%%%%%%%%%%%%%%%%%%%%%%%%%%%%%%%%%%%%%%%%%%%%%%%%%%%%%%%%%%%%%%%
% END OF THE PROGRAM TO TAKE THE FFT OF THE DATA
%%%%%%%%%%%%%%%%%%%%%%%%%%%%%%%%%%%%%%%%%%%%%%%%%%%%%%%%%%%%%%%%%%%%%%%%
```

VITA

Name:	Travis J. King
Mailing Address:	5045 Emerging Technologies Building c/o Dr. Gerard L. Coté Texas A&M University College Station, TX 77843
Email Address:	tjamal003gmail.com
Education:	B.S., Biomedical Engineering, Louisiana Tech University, 2009 M.S., Biomedical Engineering, Texas A&M University, 2011